RSC Sustainability

ROYAL SOCIETY OF CHEMISTRY

PAPER

View Article Online
View Journal | View Issue

Cite this: *RSC Sustainability*, 2025, **3**, 5609

Green synthesis of ZnO and α-Fe_2O_3 nanoparticles using Chinese fan palm leaf extract for their biological and photocatalytic activity evaluation

Ekhlakh Veg,[ab] Azam Raza,[c] Smita Rai,[d] Pratibha Bansal,[e] Swati Sharma,[d] Nidhi Mishra,[f] Riya Gupta,[e] Shivam Mishra,[g] Seema Joshi,[b] Abdul Rahman Khan[a] and Tahmeena Khan *[a]

This study presents the green synthesis of zinc oxide (ZnO) and hematite (α-Fe_2O_3) nanoparticles (NPs) using *Livistona chinensis* (Chinese fan palm) leaf extract as a natural reducing and capping agent. The synthesized NPs were characterized by UV-vis spectroscopy, FT-IR, XRD, and FE-SEM to confirm their structural and morphological features. ZnO and α-Fe_2O_3 NPs exhibited UV absorption peaks at 377 nm and 418 nm, respectively. FT-IR analysis showed characteristic Zn–O and Fe–O stretching bands at 513 cm^{-1} and 574 cm^{-1}. The average crystallite size of ZnO NPs was 25.40 nm, and that of α-Fe_2O_3 NPs was 12.37 nm. FE-SEM images revealed the triangular-shaped morphology of ZnO NPs, whereas α-Fe_2O_3 NPs were spherical. Both NPs demonstrated significant antibacterial activity. ZnO NPs showed inhibition zones of 15 ± 0.20 and 15 ± 0.90 mm against *M. luteus* and *S. abony* at 50 μg mL^{-1}, while α-Fe_2O_3 NPs were more effective against *B. subtilis*, *S. aureus*, and *E. coli* at 100 μg mL^{-1} dose concentration. Antibiofilm activity was also confirmed against *B. subtilis*, and moderate antioxidant activity *viz.* 48.63% for ZnO NPs and 36.79% α-Fe_2O_3 NPs was obtained through DPPH assay. ZnO NPs achieved 79% photocatalytic degradation against malachite green (MG) dye in 90 minutes under visible light, compared to 68% by α-Fe_2O_3 NPs. Molecular docking studies revealed favourable interactions with bacterial quorum-sensing proteins; particularly, α-Fe_2O_3 NPs exhibited strong binding affinity with LasI protein (−10.33 kcal mol^{-1}). These results suggest that the synthesized NPs hold promise for medicinal and environmental applications.

Received 18th May 2025
Accepted 14th October 2025

DOI: 10.1039/d5su00349k

rsc.li/rscsus

Sustainability spotlight

The plant-based synthesis of nanoparticles (NPs) not only averts the release of hazardous chemicals, but it is also cost- and time-effective. The present study reports the synthesis of two important NPs of ZnO and α-Fe_2O_3 mediated by *Livistona chinensis* (Chinese fan palm). The plant is known for its ornamental purpose but remains underexplored for its medicinal and other benefits. The NPs were synthesised through a facile and sustainable route in basic medium, which did not involve harsh conditions. The NPs were obtained in excellent yield. The antibacterial, antioxidant, and antibiofilm activities proved their worth as potent medicinal moieties that could be further explored as drug delivery agents. Their interactions with three important quorum-sensing proteins, *viz.*, LasR and LasI proteins of *Pseudomonas aeruginosa*, and the AgrA protein of *Staphylococcus aureus* were investigated. The docking results with α-Fe_2O_3 NPs were quite promising and exhibited good anti-biofilm activity. The role of the NPs in environmental applications, *viz.*, photocatalytic dye degradation was also studied against Malachite Green (MG) dye as the model pollutant. The photocatalytic potential of the ZnO NPs against MG dye was revealed when they showed 79% photodegradation after 90 minutes when exposed to visible light, while α-Fe_2O_3 NPs showed only 68% photodegradation efficiency. The low cost and easy availability of the plant could be exploited for the scalability of NPs. It has been found that metallic NPs are more stable as compared to those produced by other biological means, as plant extracts can reduce metal ions in a faster manner than fungi or bacteria, and they are used easily and safely for large-scale production of well-dispersed NPs. Biomolecules like proteins/enzymes, amino acids, polysaccharides, *etc.*, could be responsible for the bioreduction, formation and stabilization of metal NPs. The content of polyphenols, enzymes and chelating agents present in plants may also have critical effects on the quality and quantity of NPs. The phytoconstituents may have acted as both capping and reducing agents that stabilize the NPs as well. Overall, the study was undertaken to promote sustainable chemistry practices and was aligned with the Sustainable Development Goals (SDGs) 12 (Responsible Consumption and Production), 13 (Climate Action) and 15 (Life on Land).

[a]*Department of Chemistry, Integral University, Lucknow, Uttar Pradesh, 226026, India. E-mail: tahminakhan30@yahoo.com*

[b]*Department of Chemistry, Isabella Thoburn College, Lucknow, Uttar Pradesh, 226007, India*

[c]*Interdisciplinary Nanotechnology Centre, Zakir Husain College of Engineering and Technology, Aligarh Muslim University, Aligarh-202002, Uttar Pradesh, India*

[d]*Department of Biosciences, Integral University, Lucknow, Uttar Pradesh, 226026, India*

[e]*Department of Chemistry, University of Lucknow, Lucknow, Uttar Pradesh, 226007, India*

[f]*Department of Applied Sciences, Indian Institute of Information Technology, Prayagraj, Uttar Pradesh, 226007, India*

[g]*Department of Zoology, S.S. Khanna Girls' Degree College, Prayagraj, Uttar Pradesh, 211003, India*

1. Introduction

When compared to their bulk counterparts, nanomaterials behave differently due to their high surface-to-volume ratio, shape, size, and composition.[1] Photodegradation catalysis,[2] biomedical sensing, imaging, diagnostics, and as therapeutic agents[3–5] are among the important applications of metal and metal oxide-based nanoparticles (MONPs). Ag, Cu, and Au are the three most important metals explored to synthesize NPs.[6] When various organic ligands functionalize these nanomaterials, their therapeutic properties are improved.[7] Various methods, including physical, chemical, and biological ones, can produce nanomaterials. The physical methods are expensive and require high temperatures; the conventional chemical methods also require hazardous chemicals and organic solvents. The green synthesis is a simple, quick, and ecologically sustainable process.[8] Plant extracts, which are composed of enzymes and phytochemicals, serve as capping and reduction agents to help in the synthesis of NPs. Several variables, including pH, temperature, solvent, and the phytochemicals found in plant extracts, play an important role.[9,10] It is quite interesting to use metal-based NPs and their oxides. Zinc has significant reduction abilities and is an active element. As one of the most essential trace elements, zinc significantly affects human health. Almost all of the human body's tissues have zinc-containing enzymes.[11] ZnO behaves as an n-type semiconductor having a high binding energy (60 meV)[12,13] and does not undergo any dislocation or degradation during use.[14] These NPs can be used for biosensing due to a band gap of 3.1–3.3 eV, which shows a semiconducting nature.[15] They are also recognized for having minimal electrical conductivity and exceptional heat resistance. ZnO NPs have been produced by various techniques, like hydrothermal, direct precipitation, co-precipitation, and sol–gel solvothermal methods.[16] Several biological activities including antioxidant, antimicrobial and anticancer have been associated with ZnO NPs.[17] Bacterial antibiotic resistance is a major threat to global health care. ZnO NPs have shown good antibacterial activity against both types of bacterial strains.[18] Recent studies have demonstrated the effectiveness of plant-based extracts and other bio-reducing agents in producing functional ZnO NPs with promising photocatalytic and antimicrobial properties. For instance, ZnO NPs synthesized using *Garcinia mangostana* fruit pericarp extract were predominantly spherical (~21 nm) and exhibited excellent photocatalytic degradation of MG dye under solar irradiation, attributed to their high purity and small size.[19] Similarly, *Cucurbita* seed extract-mediated ZnO NPs showed diverse morphologies such as rods and hexagons with notable antimicrobial activity against *E. coli*, *B. pumilus*, and *S. typhi*, as well as antifungal, antioxidant, and larvicidal properties. These findings highlight the multifunctional nature of biologically synthesized ZnO NPs.[20] In another study, microwave-assisted green synthesis using starch and glucose as capping and reducing agents produced highly crystalline ZnO NPs (crystallite size ~24.4 nm) with spherical morphology. These NPs displayed significant antibacterial and antibiofilm activity, along with efficient photocatalytic degradation of methylene blue dye.[21] ZnO NPs produced using the sol–gel process showed considerable antibacterial properties. The NPs' size had a significant effect on their antibacterial activity, which improved as particle size decreased.[22] Urge *et al.* studied the antibacterial properties of ZnO NPs produced from the extracts of *Allium sativum* and *Zingiber officinale*. The NPs produced using a combination of the two extracts exhibited the strongest inhibitory zone against *P. putida* (28.67 ± 0.82 mm) and *S. pyogenes* (10.67 ± 0.47 mm).[23] Prashanth *et al.* produced Ni/Mn co-doped ZnO NPs using *Simarouba glauca* extract, showing impressive anti-tubercular activity. The *M. tb* H37Ra strain was inhibited at a minimum inhibitory concentration (MIC) of 6.25 μg mL^{-1} using both undoped and co-doped NPs.[24] Overproducing free radicals in the body results in oxidative stress and damages biomolecules if the body's antioxidant defences are compromised. Antioxidant molecules squelch these free radicals. Because of their antioxidant properties, the produced ZnO NPs can be used in the treatment of numerous oxidative stress-related disorders.[25] Another important application of metal oxide-based nanomaterials is in wastewater treatment, such as photocatalytic dye degradation.[26] The production of highly reactive hydroxyl ($OH^{\bullet}$) radicals by an appropriate photocatalyst in the presence of light radiation can convert water contaminants like various hazardous dyes into comparatively harmless end products such as CO_2, H_2O, and other inorganic ions. Therefore, these are used in the photocatalytic dye degradation process.[27] MG, a hazardous cationic colouring dye found in contaminated water bodies, belongs to the group of dyes called triphenylmethane dyes, which are used extensively in the food, printing, leather, textile, paper, plastic, pharmaceutical, and medical laboratory industries. Its chemical formula is $C_{52}H_{54}N_4O_{12}$. MG has a prominent absorption band at 617 nm.[28] It can have mutagenic, carcinogenic, and teratogenic effects on both humans and animals because of the highly toxic, hormone-disrupting, and carcinogenic compounds utilized for producing this hazardous dye colour.[29] Recently, Chinese fan palm seed biochar was used to adsorb MG dye with a maximum of 21.4 mg g^{-1} of malachite green loading (Qm) being attained.[30] Recently, ZnO NPs synthesized from *Olea europaea* fruit extract were effectively biosynthesized using a one-pot sustainable approach. The photocatalytic activity of the generated catalysts was assessed against methyl orange (MO) and methylene blue (MB) in the presence of sunlight. Degradation efficiencies of 75% and 87% were obtained in 180 minutes for MB and MO, respectively, with photodegradation rate constants (k) of 0.008 and 0.013 min^{-1}.[31] In another study, the photocatalytic activity of MG dye was done under UV light by treating with ZnO NPs obtained from *Gynostemma pentaphyllum* plant extract. 89% (10 mg L^{-1}) dye was degraded by the photocatalyst in 180 minutes.[32] In a similar study, *Punica granatum* (pomegranate) fruit peel extract was used to synthesize ZnO NPs. The NPs calcined at 700 °C showed the maximum removal effectiveness of MG dye (99%) in 40 minutes.[33] A recent study demonstrated the successful hydrothermal synthesis of 2D ZnO nanosheets, which showed high photocatalytic efficiency by degrading approximately 90% of ciprofloxacin under sunlight

within two hours. These nanosheets also exhibited notable antibacterial activity against *E. coli* and *S. aureus*, with MIC values of 5 μg L^{-1} and 10 μg L^{-1}, respectively, along with cytotoxic potential against A549 and A375 cancer cell lines. These findings highlight the multifunctionality of ZnO nanostructures in addressing environmental and biomedical challenges.[34] A recent study reported the synthesis of peony-shaped ZnO nanoflowers (ZnO-NFs) and their thorough characterization using techniques such as UV-vis spectroscopy, DLS, FTIR, and SEM. These ZnO-NFs demonstrated strong *in vitro* anticancer effects against A375 and Dalton's Lymphoma Ascites (DLA) cells, with notable dose-dependent cytotoxicity, especially toward DLA cells. The nanoflowers also exhibited excellent anti-amyloid activity at 50 μg mL^{-1}, as confirmed by ThT fluorescence, turbidity assays, and microscopy studies. Importantly, both *in vitro* and *in vivo* assessments—including fibroblast viability, hemolysis assays, and zebrafish embryo studies—confirmed their high biocompatibility up to 200 μg mL^{-1}, highlighting their potential for therapeutic use.[35]

Other than ZnO NPs, among various iron oxide NPs, in particular, hematite (α-Fe_2O_3) NPs are efficient photocatalysts due to their abundance and a suitable bandgap (1.56–2.1 eV) for sunlight absorption.[36,37] They are traditionally used in red pigments,[38] as a catalyst,[39] in electrodes,[40] as a gas sensor,[41] in magnetic materials,[42] as a photocatalyst,[43] and in anticorrosive paints. α-Fe_2O_3 NPs also find applications in solar energy conversion, pigments, high-density magnetic storage media, catalysts, water splitting, and water purification.[44] Besides these, α-Fe_2O_3 NPs have shown greater chemical stability, lower toxicity, and biocompatibility, making them more appropriate for biomedical applications.[45] When various organic ligands functionalize these metal oxide nanomaterials, their therapeutic properties improve.[7] The direct synthesis of NPs by using plant extracts has shown potential for a sustainable source of metallic NPs because of their phytochemical composition.[46] Although various variables, including pH, pressure, solvent, and others, influence the green synthesis, the phytochemicals found in plant extracts, such as ascorbic acid, phenols, carboxylic acids, terpenoids, amides, flavones, aldehydes, and ketones, play a crucial role.[47,48] Recently, CuO NPs have been produced using the plant extract from aloe vera. The band gap displayed quantum confinement due to the distinct surface structure and morphology of the NPs. Furthermore, molecular docking was carried out using AutoDock 4.2 against key proteins of *S. typhi* and *L. monocytogenes*, such as listeriolysin O, internalin (InlA), Salmonella effector protein (SopB), and YfdX, indicating potential interactions. The antibacterial activity was evaluated against *S. typhi*, *K. pneumoniae*, *P. aeruginosa*, and *L. monocytogenes*. The zone of inhibition against *S. typhi* and *L. monocytogenes* was 13 ± 0.02 and 15 ± 0.04 mm, respectively.[49] In another study, a green synthesis approach involving *Bacillus* sp. GMS10 and iron sulfate as a precursor was used to produce α-Fe_2O_3 NPs. Antibacterial studies showed that the α-Fe_2O_3 NPs had a strong effect on Gram-positive bacteria, with MIC values between 0.625 and 5 μg mL^{-1} and MBC values between 5 and 20 μg mL^{-1}.[50] Ferric chloride was used as a precursor in the phyto-mediated production of α-Fe_2O_3 NPs, mediated by *Rhus punjabensis* extract. The rhombohedral crystal structures of the produced NPs were 41.5 ± 5 nm in average size. These NPs demonstrated cytotoxic effects with ED_{50} values of 11.9 and 12.79 μg mL^{-1} against DU-145 prostate cancer and HL-60 leukemic cell lines, respectively.[45] Aida *et al.* used a simple but effective green synthesis method for producing α-Fe_2O_3 NPs utilizing a plant extract. The NPs had an average particle size of 20 nm and were polycrystalline. The produced α-Fe_2O_3 NPs exhibited superparamagnetic behaviour due to their low remnant magnetization (Mr) and saturated magnetization (Ms).[51] In another study, α-Fe_2O_3 NPs were synthesized using orange peel extract as a stabilizing agent. The synthesized NPs were examined for their antibacterial efficiency. The results indicated that the NPs were efficient against Gram-positive bacteria.[52]

In the present study, *Livistona chinensis*, commonly referred to as the Chinese fan palm, was used to produce ZnO and α-Fe_2O_3 NPs. *L. chinensis* can grow up to around 10 to 15 m (30 to 50 ft) in height and 4 m (12 ft) in spread.[53] Reducing sugars were not present in the nut extracts. The fruit and root of *L. chinensis*, are rich in flavonoids, phenolics, ceramides, and glycerides.[54] The seeds, leaves, and roots of the plant have long been used as traditional medicines to treat nasopharyngeal carcinoma, gastrointestinal cancer, and cardiovascular disease.[55] The phytoconstituents found in the plant are used as therapeutic agents for several purposes, including renal protection, cardioprotective, antimicrobial (antibacterial), cytotoxic, antipyretic, anti-inflammatory, anti-parasitic, antidiabetic, antihyperlipidemic, anticonvulsant, and cardiovascular protection.[56] Phenolic chemicals isolated from *L. chinensis* seeds have been shown in more recent investigations to exhibit a variety of biological activities.[57] Several secondary metabolites, such as vanillic acid, syringic acid, tricin, vitexin, orientin, quercitrin, orientin-7-*O*-sulfate, and many others, have been associated with the potential benefits of *L. chinensis* as given in Fig. 1.

Despite the widespread availability and traditional significance of *Livistona chinensis*, its use in the green synthesis of metal oxide NPs, particularly ZnO and Fe_2O_3 NPs has not been

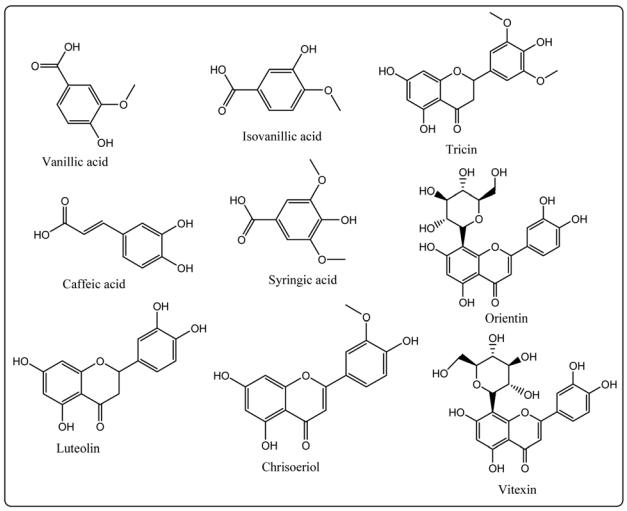

Fig. 1 Various phytochemicals found in *L. chinensis* extract.

previously reported in the literature. Most existing studies on plant-mediated NP synthesis have focused on other botanical sources, leaving a noticeable gap regarding the potential of *L. chinensis* in this field. Recently, we have also synthesised CuO and B–CuO NPs from the leaf extract of *L. chinensis*.[58] This study addresses the existing research gap by presenting, for the first time, the synthesis of ZnO and Fe_2O_3 NPs using *Livistona chinensis* leaf extract. A novel, environmentally friendly method is introduced, showcasing the plant's ability to act as a natural reducing and stabilizing agent during NP formation. By incorporating an underexplored plant species, this work broadens the scope of green nanotechnology and provides a sustainable approach for producing functional nanomaterials. The study highlights the role of phytochemicals in guiding the formation of metal oxide NPs, emphasizing their potential applications in areas such as biomedicine, catalysis, and environmental remediation. The main objectives of this work were to synthesize and characterize ZnO and α-Fe_2O_3 NPs using *L. chinensis* leaf extract and to evaluate their multifunctional properties. Specifically, the antioxidant activity was assessed using the DPPH assay, antibacterial activity was tested against selected pathogenic strains, antibiofilm potential was examined against *E. coli* and *S. aureus*, and photocatalytic performance was studied through the degradation of malachite green dye under visible light.

2. Materials and methods

Zinc chloride dihydrate ($ZnCl_2 \cdot 2H_2O$, 99.99% pure) and iron nitrate nonahydrate (Fe $(NO_3)_2 \cdot 9H_2O$, 99.99% pure) were purchased from Sigma Aldrich, Mumbai, India. Sodium hydroxide (NaOH) and MG dye were purchased from Thermo-Fischer Scientific, India. All the chemicals were used without further purification. The details of the characterization techniques used, like UV, FT-IR, XRD, SEM, and EDX, are already given in our previous study.[59] HRTEM images were captured at 200 kV using a JEOL/JEM 2100 transmission electron microscope. Liquid Chromatography-Mass Spectrometry (LC-MS/MS) analysis was done on an Agilent 6575 Triple Quadrupole. Molecular docking was done using AutoDock 4.0. The structures of the proteins were retrieved from the Protein Data Bank (PDB) and prepared using AutoDock Tools 1.5.7.

3. Experimental

3.1 Preparation of *Livistona chinensis* leaf extract

After thoroughly cleaning 80 g of fresh leaves with water, they were re-washed with deionized water. The leaves were chopped into small pieces and then dried for several days before being ground into a powder. 6 g of leaves was heated with 100 mL of deionized water for half an hour at 70 °C. The extract was cooled at room temperature, filtered using Whatman filter paper, and stored at 10 °C.

3.2 Biosynthesis of ZnO and α-Fe_2O_3 NPs

ZnO NPs were prepared by adding 20 mL of leaf extract dropwise to 80 mL of 0.1 M $ZnCl_2 \cdot 2H_2O$ solution at room temperature, with the pH adjusted to 8–10 using 0.1 M NaOH. The mixture was stirred for 1 h, yielding a yellowish-white suspension. Similarly, α-Fe_2O_3 NPs were synthesized by adding 20 mL of leaf extract to 80 mL of 0.1 M $Fe(NO_3)_3 \cdot 9H_2O$ solution, adjusting the pH to 8–10, and stirring for 2 h until a reddish-brown solution formed. In both cases, the products were centrifuged at 7000–8000 rpm for 10 minutes, washed with ethanol and water, dried at 80 °C for 2 h, and calcined at 500–600 °C for 3 h to obtain crystalline powders. Synthesis parameters such as pH, precursor concentration, and extract volume were optimized to improve yield and uniformity.[60] For extraction from plants, the pH of the mixture is a crucial factor which impacts the characteristics of the NPs.[61] An alkaline pH is required to obtain homogeneous particles with reduced agglomeration.[62] It is reported that acidic pH and neutral pH cause agglomeration of NPs in the colloidal solution. An alkaline medium boosts the surface plasmon resonance (SPR). The pH is increased due to the ionization of OH groups in the plant extract because of the biomolecules aiding the NP reduction. The colour of this combination changes to either brown or yellow, a distinct sign of NP formation.[63] The surface area of the NPs reduces with the increase in calcination temperature.[49] Previous studies have shown that crystallinity improves significantly with the rise in temperature or adequate thermal energy.[64] The schematic depiction of the synthesis of ZnO NPs and α-Fe_2O_3 NPs is presented in Fig. 2, and the probable mechanism of reactions is given as eqn (1)–(3) for ZnO NPs, and eqn (4)–(7) for α-Fe_2O_3 NPs.

$$ZnCl_2 \cdot 2H_2O(s) \xrightarrow{\text{dissolved in } H_2O} ZnCl_2(aq.) \quad (1)$$

$$ZnCl_2(aq.) \xrightarrow[\text{NaOH stirred, 1 h}]{\text{phytochemicals}} Zn(OH_2) \quad (2)$$

$$Zn(OH_2) \xrightarrow[500-600\ ^\circ C]{\text{calcined, 3 h}} \text{ZnO NPs} \quad (3)$$

$$Fe(NO_3)_3 \cdot 9H_2O \xrightarrow{\text{dissolved in } H_2O} Fe^{3+}(aq.) + 3NO_3^- + 9H_2O \quad (4)$$

$$Fe^{3+}(aq.) + 3OH^- \xrightarrow[\text{NaOH, 2 h}]{\text{Phytochemicals}} Fe(OH_3)(s) \quad (5)$$

$$Fe(OH_3)_3(s) \rightarrow FeOOH(s) + H_2O \quad (6)$$

$$FeOOH(s) \xrightarrow[500-600\ ^\circ C]{\text{calcined, 3 h}} Fe_2O_3 \text{ NPs} \quad (7)$$

3.3 Antibacterial activity evaluation, including media preparation and sterilization

The antibacterial activity of ZnO NPs was evaluated using the agar well diffusion method.[65] Bacteria were inoculated in nutrient broth and incubated at 37 °C for bacterial cell growth, and bacterial cultures were evenly swabbed onto Mueller–Hinton agar (MHA) plates, and wells with a diameter of 5 mm were filled with various concentrations of the sample. The bacterial

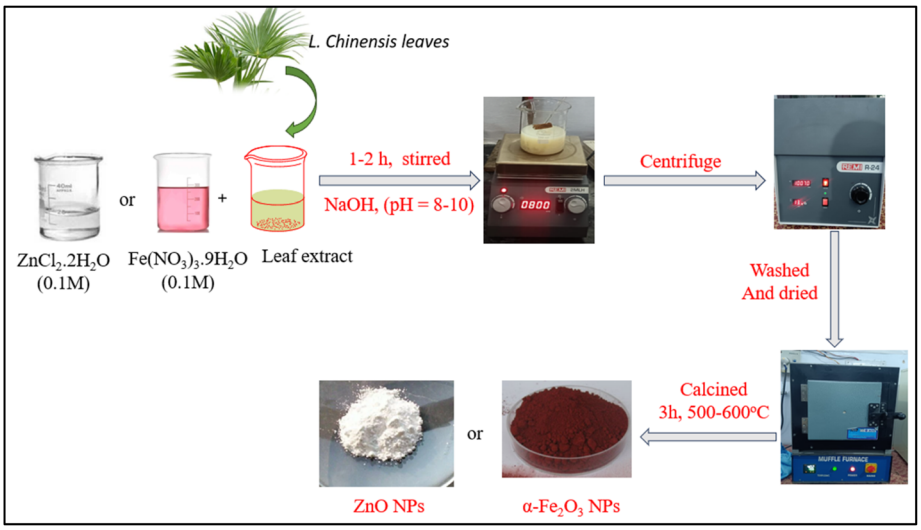

Fig. 2 Schematic representation of the synthesis of ZnO and α-Fe_2O_3 NPs.

cell suspensions were adjusted to an optical density of 0.1 at 600 nm using a spectrometer (Eppendorf, AG, Germany), corresponding to approximately 10^8 colony-forming units per millilitre (CFU mL^{-1}). Different concentrations of NPs (25, 50, 75, and 100 μg mL^{-1}) were tested for their inhibitory effects. Gentamycin (1 μg mL^{-1}) served as the positive control in the experiment. The antibacterial activity and MIC were assessed in triplicate. The Petri plates containing the sample were kept at 37 °C in an incubator and monitored for up to 24 h; it was sealed with parafilm to prevent contamination and maintain sterility.

3.4 Antibiofilm formation

The antibiofilm activity of the synthesized NPs was evaluated against *S. aureus* and *E. coli* following reported procedures with slight modifications. Biofilms were allowed to form over a period of 72–96 hours, and the disruption caused by NPs' treatment was quantified using standard crystal violet staining and microscopy-based analysis. A similar methodology was successfully applied in recent work using reduced graphene oxide nanosheets, which demonstrated significant antibiofilm disruption in *E. coli* and *S. aureus*.[66] The effect of NPs on bacterial biofilm formation was assessed using a microtiter plate (MtP) assay, as described earlier[67] and following an earlier reported approach.[59] The NPs were tested at three sub-MIC concentrations (25, 50, and 100 μg mL^{-1}), selected based on prior antibacterial assays to ensure biofilm disruption was measured under non-lethal conditions. Bacterial cultures were standardized to a 0.5 McFarland standard, diluted to ~5×10^5 CFU mL^{-1}, and incubated in Mueller–Hinton Broth (MHB). Biofilms were allowed to form for 18–24 h at 37 °C, which represents the physiological growth temperature of these pathogens. Following incubation, biofilms were stained with 0.1% crystal violet for 20 minutes. Excess stain was removed by washing with PBS (pH 7.4), which maintains physiological ionic balance during rinsing. The retained dye was solubilized in 95% ethanol, and absorbance was recorded at 570 nm using a Biored iMark microplate reader (USA). All experiments were performed in triplicate, and inhibition percentages were calculated relative to untreated controls using eqn (8).

$$\text{Percentage of inhibition} = 100 - [(OD_{570\ nm}\ \text{of the treated wells})/(\text{mean } OD_{570\ nm}\ \text{of the negative control wells containing no antimicrobial agent}) \times 100] \quad (8)$$

3.5 Assessment of antioxidant activity using DPPH radical scavenging assay (RSA)

The antioxidant activity was assessed using the DPPH radical scavenging assay.[59] A 0.1 mM DPPH stock solution was prepared in ethanol, as this concentration provides stable absorbance at 517 nm. Different concentrations of ZnO NPs (25, 50, 100, 150, and 200 μg mL^{-1}) were tested, while ascorbic acid (12.5–200 μg mL^{-1}) served as the positive control. For each reaction, 3 mL of the DPPH solution was mixed with the test sample and incubated in complete darkness for 30 minutes to prevent light-induced degradation of DPPH. The decrease in absorbance was measured at 517 nm, corresponding to the absorption maximum of DPPH. Radical scavenging activity (RSA, %) was calculated using eqn (9).

$$\%\ \text{of antioxidant activity} = [(A_c - A_s) \div A_c] \times 100 \quad (9)$$

where A_c = absorbance of the control, A_s = absorbance of the test sample.

3.5.1 Statistical analysis. All experiments were carried out with at least three independent biological replicates, and the results are expressed as mean values ± standard error of the mean (SEM). Each point in the figures corresponds to the average of three replicates, with error bars indicating SEM. Statistical evaluation was performed using two-way ANOVA followed by multiple comparison tests, and differences were considered statistically significant at $P < 0.05$.

3.6 Photocatalytic dye degradation assessment

The photocatalytic dye degradation was done as per the procedure followed in our previous manuscript.[59] The percentage degradation of the dye was calculated using eqn (10).

$$\% \text{ Degradation} = (A_0 - A_t)/A_0 \quad (10)$$

where A_0 represents the dye absorbance at the beginning and A_t represents the dye absorbance at time t.

The kinetics of the degradation were also studied by plotting $\ln(C_o/C_t)$ against time. The kinetic study was done by using pseudo-first-order kinetics using eqn (11).

$$\ln(C_o/C_t) = kt \quad (11)$$

Here, C_o represents the initial concentration, C_t denotes the concentration at time t, and k is the rate constant. The slope of the plot of $\ln(C_o/C_t)$ against the time gives a rate constant, k.

3.7 Molecular docking

To assess the interactions between the NPs and bacterial quorum-sensing proteins, molecular docking studies were carried out, specifically the LasR (PDB ID: 4NG2) and LasI(PDB ID: 1RO5) proteins of *P. aeruginosa*, and the AgrA protein of *S. aureus* (PDB ID: 4 G4K). The NPs were used as the ligand in all docking simulations.

3.7.1 Protein and ligand preparation. To make the proteins more suitable for docking, polar hydrogens have been included, and water molecules have been eliminated. The NPs' crystal structure was retrieved from the Materials Project database (**https://next-gen.materialsproject.org**) using the material ID mp-1986, and the standard inhibitor gingerol was retrieved from PubChem. Both were prepared by assigning Gasteiger charges, and all torsions were fixed, followed by energy minimization, saved in pdbqt format for molecular docking. The active sites of the proteins were identified, and grid boxes were defined around these regions to facilitate precise docking. The Lamarckian genetic algorithm was employed with default parameters, running 10 docking simulations for each protein–ligand pair. Binding energy values (kcal mol^{-1}) and inhibition constants (K_i) were calculated for each docked complex. The resulting docked conformations were analyzed for hydrogen bond formation and other interactions by using Discovery Studio and UCSF Chimaera.

4. Results and discussion

4.1 FT-IR analysis

FT-IR analysis was done between 4000 and 400 cm^{-1}. The FT-IR spectrum of the leaf extract (Fig. 3) showed major broad peaks at 3250–3350 cm^{-1} from OH groups and at 1634 cm^{-1} due to C=O groups of the phytochemicals.[68] The stretching frequency of the water hydroxyl group that was adsorbed on the surface of ZnO NPs during the investigation was identified at 3385 cm^{-1} (ref. 69) while in the case of α-Fe_2O_3 NPs, a band at 3419 cm^{-1} represented the stretching frequency of the OH group of water, which might be due to moisture on the surface of the NPs, as found in previous work.[70] Furthermore, a new peak at 513–535 cm^{-1} confirmed the formation of the Zn–O bond[71] while Fe–O vibrations were observed at 574 cm^{-1}, indicating the formation of α-Fe_2O_3 NPs.[72] The peak at 1520 cm^{-1} was attributed to the aromatic nitro compounds. Vinyl C–H in-plane bending was observed at 1407 cm^{-1}, whereas the peak at 875 cm^{-1} was due to the C=C–C aromatic ring stretching.[73] Similarly, iron oxide NPs showed C–O stretching in the frequency range of 1340 and 1523 cm^{-1}, and C=O stretching at 1630 cm^{-1} due to the presence of phenolic and flavonoid compounds with carbonyl and hydroxyl groups as functional groups. Additionally, in α-Fe_2O_3 NPs, an intense peak at 2350 cm^{-1} was observed, which might be due to the formation of carboxylates on their surface.[74]

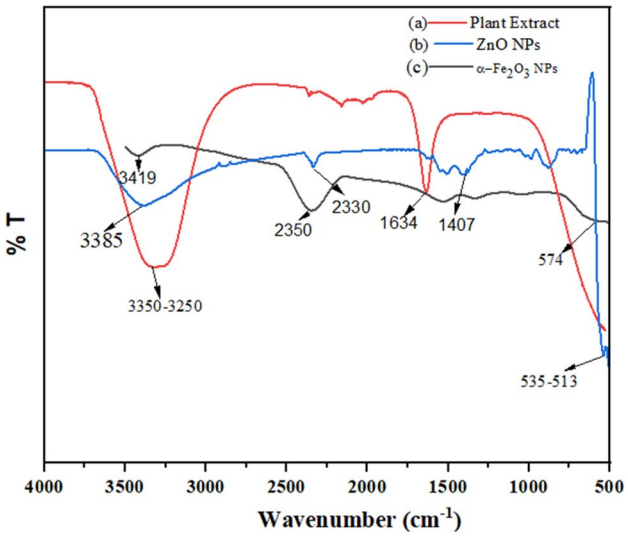

Fig. 3 FT-IR spectra of (a) *L. chinensis* leaf extract, (b) ZnO NPs and (c) α-Fe_2O_3 NPs.

4.2 XRD analysis

XRD analysis was conducted on the dried powdered samples, revealing prominent diffraction peaks at 2θ values of 31.14° (100), 33.84° (002), 35.78° (101), 46.90° (102), 56.20° (110), 62.50° (103), 65.88° (200), 67.66° (112), 68.62° (201), 72.10° (004), and 76.46° (202). These peaks correspond well with the standard (PDF # 96-900-4181), confirming the formation of pure ZnO NPs with a hexagonal wurtzite structure. The lattice constants were calculated as $a = 3.2530$ Å, $c = 5.2070$ Å ($\alpha = 90°$, $\gamma = 120°$),[75] consistent with reported ZnO values. The average sizes of the NPs were calculated using Scherrer's equation (eqn (12)) and are given in Tables 1 and 2.

$$D = \frac{k\lambda}{\beta \cos \theta} \quad (12)$$

where D is the average crystallite size, $K = 0.9$ (shape factor), $\lambda = 1.5406$ Å (Cu Kα radiation), β is the full width at half maximum (FWHM) in radians (after correcting for instrumental broadening), and θ is the Bragg angle. A similar study examined the XRD pattern of ZnO NPs generated from *Phoenix dactylifera* fruit extract. ZnO NPs' hexagonal wurtzite phase has been related to

Table 1 Crystallite size, strain, and dislocation density of ZnO NPs

Peak (*hkl*)	2θ (°)	θ (°)	Crystallite size D (nm)	Lattice strain ($\varepsilon \times 10^{-3}$)	Dislocation density δ ($\times 10^{15}$ lines m^{-2})	Average crystallite size (nm)
(100)	31.14	15.57	19.30	2.4	2.7	25.40
(002)	33.84	16.92	21.70	2.0	2.1	
(101)	35.78	17.89	24.10	1.8	1.7	
(102)	46.90	23.45	28.70	1.6	1.2	
(110)	56.20	28.10	33.20	1.4	0.9	

each of the diffraction peaks in the spectrum.[76] The XRD spectra of the synthesized ZnO NPs and α-Fe_2O_3 NPs are given in Fig. 4(a) and (b), respectively.

The average crystallite size of the ZnO NPs was calculated using the Scherrer equation, corrected for instrumental broadening, and found to be ~25.40 nm (Table 1). In addition, the lattice strain (ε) was estimated using eqn (13):

$$\varepsilon = \frac{\beta}{4 \tan \theta} \tag{13}$$

The dislocation density (δ) was calculated using eqn (14):

$$\delta = \frac{1}{D^2} \tag{14}$$

where D is the crystallite size. The calculated values indicate a strain in the order of 10^{-3}, with dislocation density ~1.5 × 10^{15} lines m^{-2}, suggesting slight lattice distortions associated with the nanoscale crystallites. These results confirm the good crystallinity of the ZnO NPs obtained after annealing at 500 °C.

To ensure accuracy, instrumental broadening was subtracted using a standard Si reference material, as per the following eqn (15):

$$\beta = \sqrt[2]{\beta_{\text{observed}}{}^2 - \beta_{\text{instrumental}}{}^2} \tag{15}$$

For α-Fe_2O_3, the XRD peaks observed at 31.05°, 32.55°, 35.05°, 44.86°, 53.51°, and 74.93° matched the JCPDS card (no. 33-0664), confirming the rhombohedral hexagonal phase.[77] The calculated average crystallite size was ~12.41 nm (Table 2).[78] The lattice constants were determined to be $a = 5.038$ Å and $c = 13.772$ Å, consistent with standard hematite values. The calculated strain was ~2×10^{-3} with dislocation density ~6.5×10^{15} lines m^{-2}. Previously synthesized α-Fe_2O_3 NPs using *Tabebuia aurea* leaf extract had an average crystallite size of 25.69 nm.[79] Balu *et al.* have also synthesized α-Fe_2O_3 from *Raphanus sativus* leaf extract, and the size of NPs was found to be 48.19 nm with a rhombohedral structure.[80]

Table 2 Crystallite size, strain, and dislocation density of α-Fe_2O_3 NPs

Peak(*hkl*)	Peak 2θ (°)	Crystallite size D (nm)	Lattice constants (a, c Å)	Lattice strain ($\varepsilon \times 10^{-3}$)	Dislocation density δ ($\times 10^{15}$ lines m^{-2})	Average crystallite size (nm)
(104)	31.05	11.32	$a = 5.038$, $c = 13.772$	2.1	7.8	12.41
(110)	32.55	11.46	$a = 5.038$, $c = 13.772$	2.0	7.6	
(113)	35.05	9.72	$a = 5.038$, $c = 13.772$	2.4	10.6	
(024)	44.86	12.48	$a = 5.038$, $c = 13.772$	1.9	6.4	
(116)	53.51	13.75	$a = 5.038$, $c = 13.772$	1.7	5.3	
(300)	74.93	15.78	$a = 5.038$, $c = 13.772$	1.5	4.0	

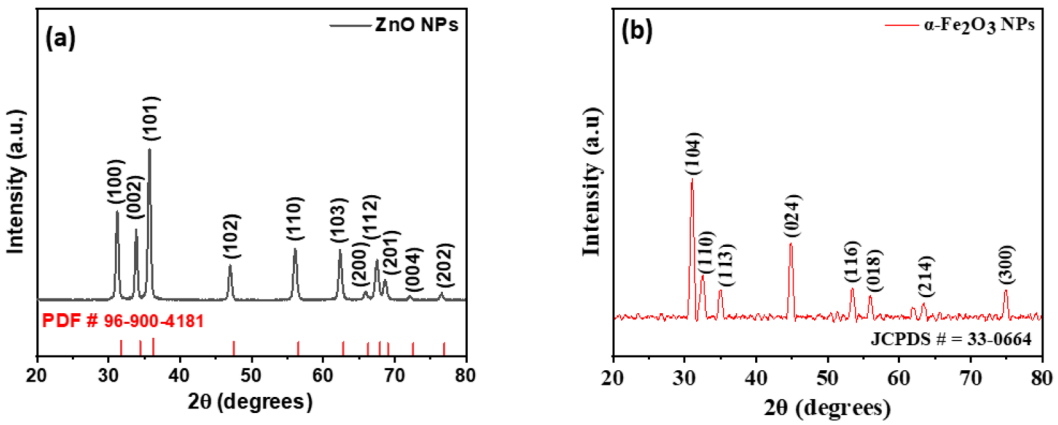

Fig. 4 XRD spectra of (a) ZnO NPs and (b) α-Fe_2O_3 NPs.

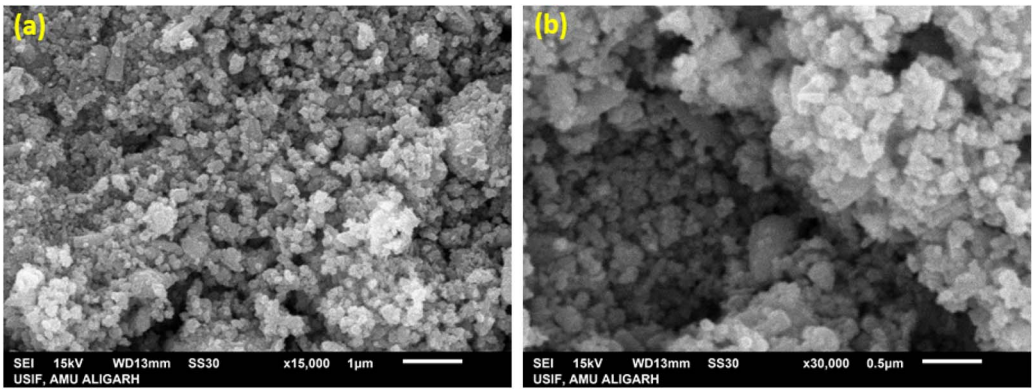

(a) (b)

Fig. 5 (a and b) FE-SEM images of ZnO NPs at (a) 15 kx and (b) 30 kx.

Thus, the inclusion of structural parameters strengthens the XRD analysis, providing a more detailed insight into the crystallinity, lattice dimensions, and defect density of the biosynthesized ZnO and α-Fe_2O_3 NPs.

4.3 Morphological studies

The surface morphology of the ZnO NPs obtained by the green synthesis was analyzed by FE-SEM as shown in Fig. 5(a) at 50 kx and Fig. 5(b) at 100 kx magnification, respectively. The FE-SEM analysis revealed the formation of non-spherical NPs, which contain numerous smaller clusters of NPs due to the agglomeration, because they tend to reduce the high surface energy as they grow. In the case of α-Fe_2O_3 NPs, as shown in FE-SEM images (Fig. 6), the formation of spherical nanoclusters was revealed, which contained numerous smaller NPs ascribed to NP aggregation. Using EDX analysis, the synthesized NPs' elemental composition was also assessed (Fig. 7(a)). The high purity of the produced ZnO NPs was confirmed by the EDX data, showing the appropriate phase of Zn and O present in the sample. The elemental composition of zinc and oxygen was 77.33 and 22.67% by weight, and 45.50 and 54.50% by atom, respectively. EDX demonstrated the purity of the NPs' produced hematite phase, which contained about 28.76% Fe and 71.24% O (Fig. 7(b)). No additional peaks were observed, which indicates the purity of the NPs. The NPs get aggregated with the increase in temperature, resulting in a larger particle size. The agglomeration and clustering of NPs is also due to high surface energy.[81] The size of the NPs obtained from SEM microscopy was greater than that obtained from the Scherrer equation. This also reveals the polycrystallinity of the sample, enclosing around ~36 nm crystallite grains.[82]

To further investigate the morphology and physical dimensions of the synthesized material, particle size analysis was carried out using SEM micrographs, processed with ImageJ software. The particle size was calculated using ImageJ software, and the average particle sizes were found to be ~32.50 nm for α-Fe_2O_3 NPs and ~37.50 nm for ZnO NPs. TEM micrographs are presented in Fig. 8(a) and (b) for α-Fe_2O_3 and Fig. 8(d) and (e) for ZnO. Furthermore, the particle size distribution histograms, shown in Fig. 8(c) for α-Fe_2O_3 NPs and Fig. 8(f) for ZnO NPs, confirmed the narrow size distribution of the NPs. The difference between crystallite size and

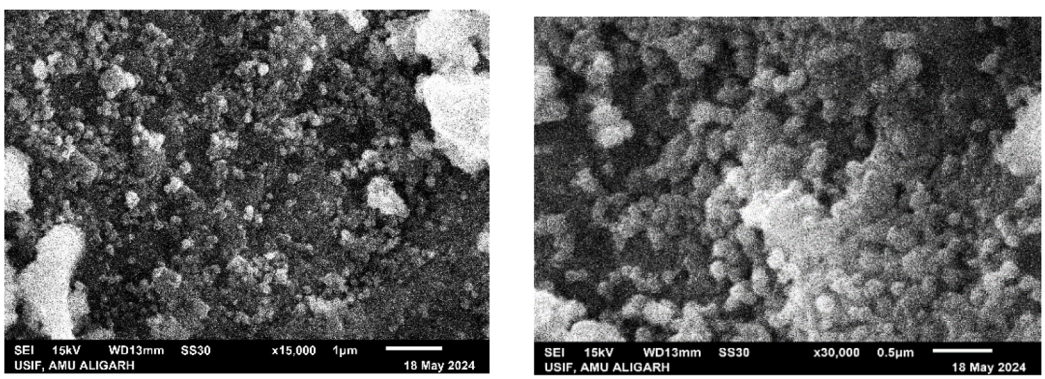

(a) (b)

Fig. 6 (a and b) FE-SEM image of α-Fe_2O_3 NPs at (a) 15 kx and (b) 30 kx.

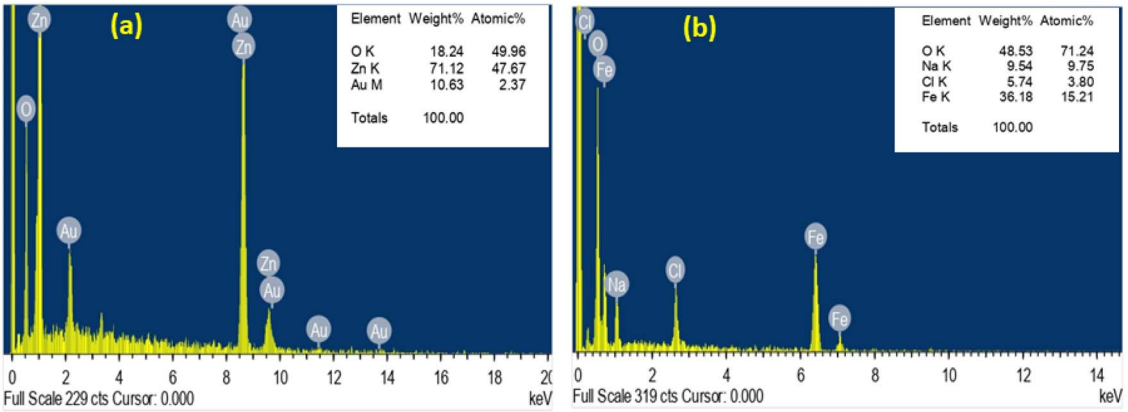

Fig. 7 EDX analysis of (a) ZnO NPs and (b) α-Fe_2O_3 NPs.

particle size is consistent with the nature of polycrystalline materials. The crystallite size obtained from XRD reflects the size of coherently diffracting domains, *i.e.*, regions within a particle that are structurally continuous and free from grain boundaries. This discrepancy suggests that each NP likely consists of multiple crystallites, indicating agglomeration or a polycrystalline nature as depicted in the SEM image. This combined approach, including XRD for crystallite size and SEM/ImageJ for particle size, provides a more comprehensive understanding of the morphology and structure of the NPs obtained by the green synthesis.

4.4 Optical properties

The band gap energy (E_g in eV) was determined by using Tauc's eqn (16).

$$\alpha h\nu = K(h\nu - E_g)^n \quad (16)$$

where h is Planck's constant, E_g is the band gap, and n is a constant.

ZnO NPs showed an absorption peak at 377 nm (Fig. 9(a)), while α-Fe_2O_3 NPs exhibited a peak at 362 nm (Fig. 10(a)), both attributed to surface plasmon resonance. In metal oxide NPs, this phenomenon arises from the collective oscillation of conduction electrons under incident electromagnetic radiation, particularly when the light wavelength exceeds the particle size.[83] The band gap was calculated using $(\alpha h\nu)^2$ and found to be 2.98 eV for ZnO NPs (Fig. 9(b)) and 2.01 eV for α-Fe_2O_3 NPs (Fig. 10(b)). The observed shift in band gap (bulk ZnO: ~3.28 eV; α-Fe_2O_3: ~2.25 eV) compared to bulk values is attributed to the quantum confinement effect and reduced particle size, which alter the electronic structure. The reduction in band gap may result from oxygen vacancies, which introduce defect states within the band structure and lower the overall band gap of the NPs.[84]

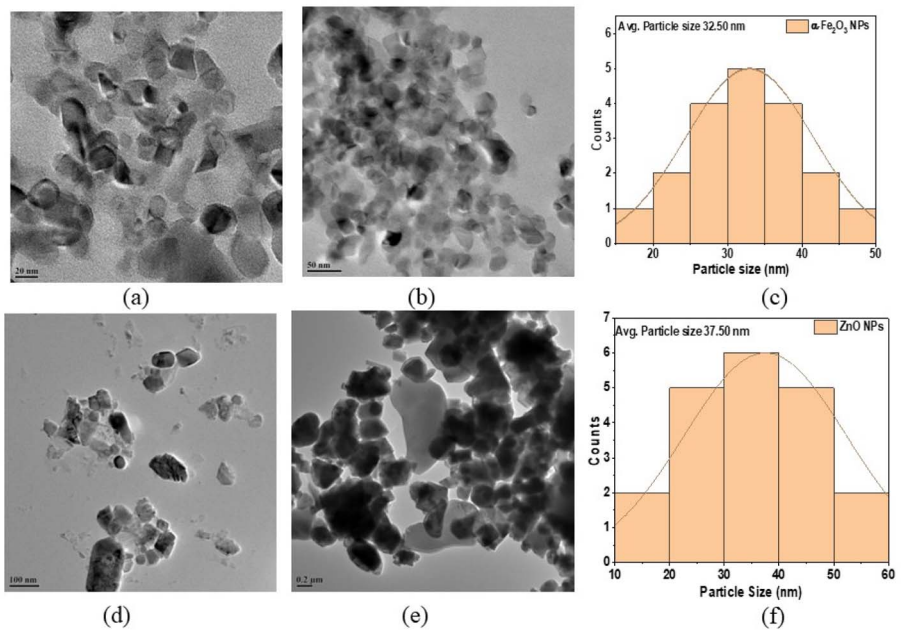

Fig. 8 TEM images and particle size distribution (calculated using Image J software) of (a–c) α-Fe_2O_3 NPs, and (d–f) ZnO NPs.

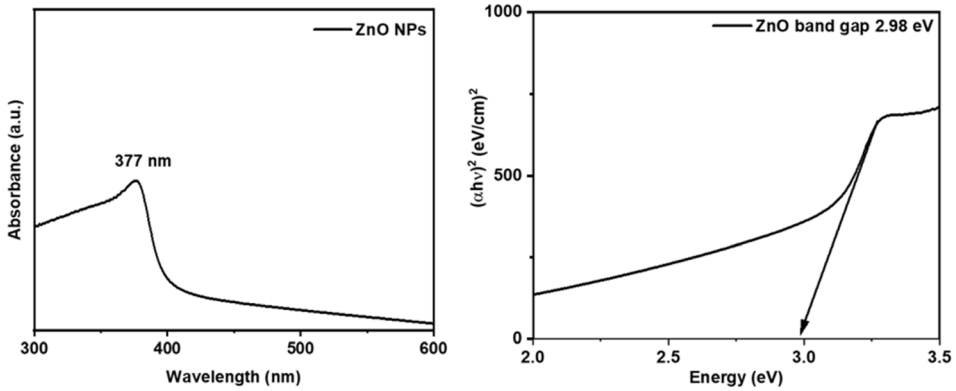

Fig. 9 (a) UV-visible absorption spectrum and (b) calculated band gap of ZnO NPs.

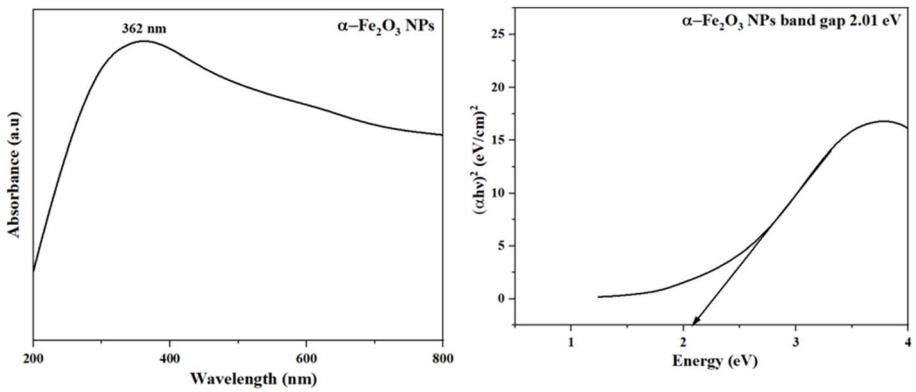

Fig. 10 (a) UV-visible absorption spectrum and (b) calculated band gap of α-Fe_2O_3 NPs.

4.5 Antibacterial activity evaluation

Several metal and metal oxide NPs, such as Ag_2O, ZnO, CuO, Al_2O_3, and TiO_2 have been tested for their antibacterial or bactericidal properties.[85,86] The highest zone of inhibition (mm) was found against *M. luteus* (17 ± 0.16) and *S. abony* (16 ± 0.80) at a concentration of 100 μg mL^{-1}, while the least was found against *E. coli* (12.06 ± 0.04) and *B. subtilis* (13.06 ± 0.09) mm, respectively, at the same concentration, Table 3 and Fig. S1(a–f) given in the SI file. At a lower concentration of NPs (50 μg mL^{-1}), the zone of inhibition against *M. luteus* and *S. abony* was 15 ± 0.20 mm and 15 ± 0.90 mm, respectively (Table 3). The findings were in line with previous studies. For instance, the aqueous leaf extract of *E. colona* was used to synthesize ZnO NPs, which exhibited antibacterial efficacy against *M. luteus* and *K. pneumoniae*, with the highest zones of inhibition measuring 17 and 18 mm, respectively.[87] The literature also supports the observation that NPs obtained by a green synthesis have better activity as compared to their chemical counterparts. The size and shape of ZnO NPs also affect the antibacterial activity.[88] For instance, ZnO NPs synthesized from *Leonotis ocymifolia* had smaller crystallite sizes (18.24–19.32 nm) than their chemically synthesized counterparts (21.50 nm), and were more efficient against *S. aureus* than *E. coli*.[89] The efficacy of plant-mediated ZnO NPs against *S. aureus* has also been established in different studies.[90,91] In the case of Fe_2O_3 NPs, the zone of inhibition (mm) was highest against *E. coli* (21 ± 0.13) at a concentration of 100 μg mL^{-1}, while the least activity was found against *M. luteus* and *S. abony*, *viz.*, 13 ± 0.07 and 13 ± 0.09 mm, respectively. The NPs exhibited appreciable inhibition against *E. coli* (18 ± 0.10 mm) than the standard (15 ± 0.09). The zone of inhibition (mm) of the synthesized α-Fe_2O_3 NPs and agar plates has been shown in Table 4 and Fig. S2(a–f) given in the SI file. Previous studies have also confirmed the antibacterial properties of Fe_2O_3 NPs, which were made with extract from the leaves of *Piper betle* and tested using the agar well diffusion method against *S. aureus*, *S. mutans*, *E. coli*, and *P. aeruginosa*. The NPs showed lesser antibacterial activity against *Streptococcus mutans* (11 mm), and higher activity against *P. aeruginosa* (15 mm) at 1000 μg mL^{-1}.[92] Fe_2O_3 NPs may be a significant generator of ROS that inhibits the growth of bacteria. Selvanathan *et al.* prepared ZnO NPs through a sustainable green synthesis approach utilizing *Annona muricata* L. (soursop) leaf extract as the reducing and stabilizing agent by microwave irradiation. The antibacterial activity of the synthesized ZnO NPs was tested against *B. subtilis*, *S. aureus*, *K. pneumoniae*, and *P. aeruginosa*. At a concentration of 10 mg mL^{-1}, the NPs showed notable inhibitory effects. These findings highlight a facile and eco-benign synthetic route for ZnO NPs with promising potential for biomedical applications.[93] The

Table 3 Zone of inhibition (mm) of the synthesized ZnO NPs

		Zone of inhibition (mm)				
		Concentration (μg mL^{-1}) of NPs			Gentamicin (standard)	Control (DMSO)
S. no.	Bacterial strain	50	75	100	50 μg mL^{-1}	50%
1	*Bacillus subtilis*	9 ± 0.18	11 ± 0.14	13 ± 0.90	27 ± 0.40	0.0
2	*Micrococcus luteus*	15 ± 0.20	15 ± 0.90	17 ± 0.16	28 ± 0.14	0.0
3	*Staphylococcus aureus*	14 ± 0.80	14 ± 0.90	15 ± 0.14	29 ± 0.90	0.0
4	*Escherichia coli*	05 ± 0.12	10 ± 0.80	12 ± 0.40	24 ± 0.80	0.0
5	*Salmonella abony*	15 ± 0.90	15 ± 0.40	16 ± 0.80	28 ± 0.80	0.0
6	*Pseudomonas aeruginosa*	14 ± 0.12	15 ± 0.40	15 ± 0.90	24 ± 0.12	0.0

Table 4 Zone of inhibition (mm) of the synthesized α-Fe_2O_3 NPs

		Concentration (μg mL^{-1})			Gentamicin (standard)	Negative control (DMSO)
S. no.	Bacterial strain	50	75	100	50 μg mL^{-1}	50%
1	*Bacillus subtilis*	16 ± 0.70	18 ± 0.80	19 ± 0.70	26 ± 0.11	0.0
2	*Micrococcus luteus*	0.0	9 ± 0.80	13 ± 0.70	27 ± 0.10	0.0
3	*Staphylococcus aureus*	14 ± 0.30	14 ± 0.60	19 ± 0.10	26 ± 0.10	0.0
4	*Salmonella abony*	0.0	10 ± 0.50	13 ± 0.90	27 ± 0.10	0.0
5	*Pseudomonas aeruginosa*	13 ± 0.80	13 ± 0.70	17 ± 0.10	25 ± 0.90	0.0
6	*Escherichia coli*	18 ± 0.10	18 ± 0.10	21 ± 0.13	15 ± 0.90	0.0

proposed mechanism involves light-activated ZnO NPs penetrating the bacterial cell wall, as observed in SEM and TEM images. These NPs disrupt the membrane, accumulate in the cytoplasm, and interact with biomolecules, ultimately inducing apoptosis and cell death.[94] In another study, ZnO NPs exhibited strong antibacterial effects against *E. coli*, even without direct cell contact. ZnO NPs disrupted bacterial membranes non-specifically, as shown by potassium leakage and liposome damage. Although small amounts of Zn(II) and H_2O_2 were present, they were not solely responsible for the antibacterial action. However, the use of radical scavengers reduced this effect, indicating that reactive oxygen species, particularly hydroxyl radicals, play a key role in the antimicrobial mechanism.[95] A probable mechanism, as discussed in the literature, shows that ZnO NPs may react with intracellular oxygen, creating oxidative stress from ROS, which can negatively impact bacterial protein and DNA activity. ZnO NPs may also damage the cell wall, which inhibits bacterial growth. Moreover, the synthesized ZnO NPs may have exerted antibacterial properties due to their small size. Similarly, α-Fe_2O_3 NPs are electrostatically attracted to the bacterial surface, the bacterial cell wall is disrupted, and its permeability increases.[96] When Fe_2O_3 NPs reacted with intracellular oxygen, oxidative stress resulted, which ultimately caused the bacterial cells' membranes to be damaged. According to Hammad *et al.*, Fe_2O_3 NPs produced from *Capparis zeylanica* leaf extract displayed zones of inhibition of approximately 23 and 22 mm, respectively, against *P. aeruginosa* and *S. aureus*.[97] Iron oxide nanoparticles (IONPs) have demonstrated interesting antibacterial activity, due to their capacity to both denature and inhibit enzyme activity. IONPs, for instance, can directly bind to enzymes, changing their three-dimensional structure, thereby affecting their functioning.[98] To prevent substrate binding and catalytic activity, the NPs may adhere to the enzyme's active sites or other critical regions.[99] According to the literature, Fe_2O_3 NPs adhered to the cell wall of *E. coli* and even entered the cytoplasm, where they aggregated inside and caused vacuole formation and cell wall disruption.[100–102] One of the potential bactericidal effects of Fe_2O_3 NPs is the production of ROS, which can damage cells in several ways, including breaking DNA strands, deactivating enzymes, and peroxidizing membrane lipids, which kills bacteria.[103] According to Arakha *et al.*, negatively charged bacterial surfaces were drawn to positively charged chitosan-coated iron oxide (Fe_3O_4/γ-Fe_2O_3) NPs. This resulted in increased ROS generation in the surrounding region of the bacterial surface. Furthermore, ROS generation in the presence of iron oxide NPs occurs due to the Fenton reaction.[104] The probable mechanism of the antibacterial activity is depicted in Fig. 11.[104]

Previously, studies have explored the antibacterial potential of metal oxide NPs produced through green synthesis, and some of the studies and their findings have been summarized in Tables 5 and 6.

4.5.1 Minimum inhibitory concentration (MIC) of ZnO and α-Fe_2O_3 NPs. For ZnO NPs *E. coli*, *S. abony*, and *P. aeruginosa* had MICs more than 0.40 μg mL^{-1}, while *B. subtilis*, *M. luteus*, and *S. aureus* had MICs lower than 0.30 μg mL^{-1}. Similarly, α-Fe_2O_3 NPs had MIC values of less than 0.40 μg mL^{-1} against Gram-positive bacteria like *B. subtilis* and *M. luteus*, and more than 0.80 μg mL^{-1} against Gram-negative bacteria, including *P.*

Table 5 Some ZnO NPs obtained by green synthesis and their antibacterial activities

S. no.	Plant source/extract	Bacterial strain	Zone of inhibition	Ref.
1	*Nauclea latifolia* fruit extract	*E. coli*	21 mm	105
		S. aureus	16 mm	
2	*Echinochloa colona* leaf extract	*E. coli*	17 mm	106
		K. pneumoniae	18 mm	
3	*Withania coagulans* extract	*S. aureus*	18 mm	107
		P. aeruginosa	13 mm	
4	*Alnus nepalensis* bark extract	*K. pneumoniae*	18 mm	108
		E. coli	23 mm	
5	*Rosa indica*	*S. aureus*	15 mm	109
		E. coli	14.5 mm	
6	*Allium cepa* L.	*P. aeruginosa*	13.17 mm	110
		E. coli	22.00 mm	
		S. aureus	12.35 mm	
7	*Cyperus scariosus*	*L. monocytogenes*	18 mm	111
		S. epidermidis	20 mm	
		E. coli	16 mm	
		B. bronchiseptica	14 mm	
8	***Livistona chinensis*** leaf extract	***B. subtilis***	**13 ± 0.90 mm**	**Present study**
		M. luteus	**17 ± 0.16 mm**	
		S.aureus	**15 ± 0.14 mm**	
		E. coli	**12 ± 0.40 mm**	
		S. abony	**16 ± 0.80 mm**	
		P. aeruginosa	**15 ± 0.90 mm**	

aeruginosa, *S. abony*, and *E. coli*. Hence, both the NPs were found to be more susceptible to Gram-positive bacteria than Gram-negative bacterial strains. A possible explanation may be that Gram-negative bacteria grow less quickly than Gram-positive bacteria as ZnO NPs' concentrations increase. Gram-positive bacteria have been proposed to be more susceptible due to differences in cell wall construction, cell physiology, metabolism, or degree of contact.[119] The MIC values can be different for different genera. As a general trend, the MIC values of NPs are lower for Gram-positive bacteria like *Micrococcus luteus* as compared to Gram-negative bacteria such as *E. coli*. This suggests that *M. luteus* is more susceptible to NPs than *E. coli*. Similar findings have been obtained previously.[120,121] The antibacterial activity of AgNPs obtained by green synthesis was tested against selected Gram-negative foodborne pathogens. Their findings also revealed that *E. coli* showed a higher MIC value compared to other Gram-negative bacteria tested, indicating a lower susceptibility to AgNPs. The MIC graph is shown in Fig. 12.

4.6 Antibiofilm potential of ZnO-NPs and α-Fe_2O_3-NPs

The results of the anti-biofilm assay showed that the synthesized ZnO NPs exhibited notable anti-biofilm activity against *B. subtilis* and *E. coli*, while α-Fe_2O_3 NPs showed significant anti-

Table 6 Some IONPs obtained by green synthesis and their antibacterial activities

S. no	Plant source	IONPs	Bacterial strains	Zone of inhibition/MIC	Ref.
1	*Platycladus orientalis*	Ce-doped- α-Fe_2O_3 NPs	*E. coli*	15.00 mm	112
2	*Sageretia thea* (Osbeck.)	α-Fe_2O_3 NPs	*P. aeruginosa*	MIC: 7.4 μg mL^{-1}	113
3	*Thymus migricus*	α-Fe_2O_3	*S. aureus*	16.15 mm	114
			S. enterica	13.31 mm	
4	*Allium sativum*	α-Fe_2O_3/MgO	*E. coli*	20 mm	115
5	*Carica papaya* Linn peel extract	Ag/Fe_2O_3–NCs	*B. cereus*	19.5 mm	116
			S. aureus	19 mm	
			S. typhi	18 mm	
			E. coli	16.2 mm	
6	Coffee seed extract	α-Fe_2O_3	*E. coli*	MIC: 50.00 μg $μL^{-1}$	117
			S. aureus	65.00 μg $μL^{-1}$	
7	Piper betel leaves	α-Fe_2O_3	*P. aeruginosa*	15 mm	118
			S. mutans	11 mm	
8	***Livistona chinensis***	α-Fe_2O_3	***B. subtilis***	**19 ± 0.70 mm**	**Present study**
			M. luteus	**13 ± 0.70 mm**	
			S. aureus	**19 ± 0.10 mm**	
			E. coli	**13 ± 0.90 mm**	
			S. abony	**17 ± 0.10 mm**	
			P. aeruginosa	**21 ± 0.13 mm**	

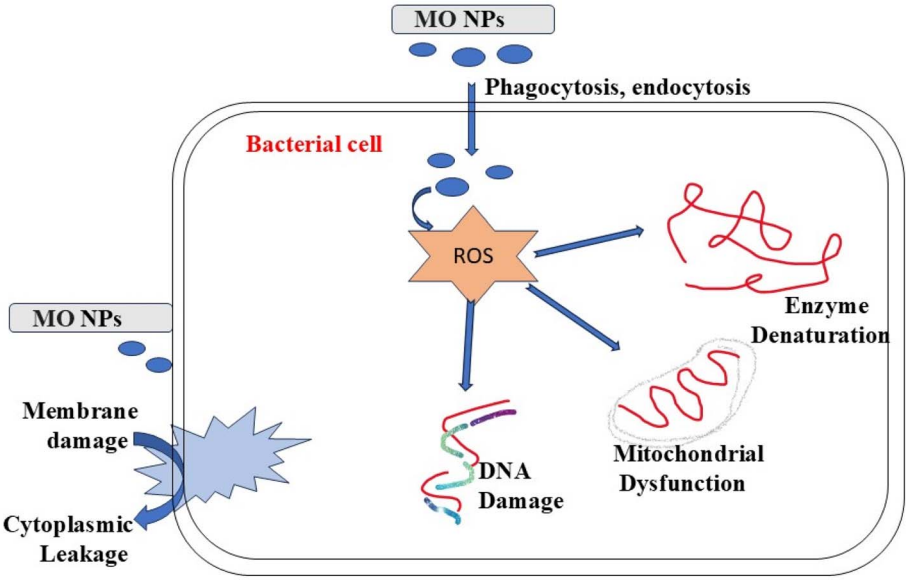

Fig. 11 Probable mechanism of antibacterial activity of MO NPs.

biofilm activity against *B. subtilis* and *S. aureus* even at concentrations below the minimum inhibitory concentration (sub-MIC) levels of 100 μg mL^{-1}, 50 μg mL^{-1}, and 25 μg mL^{-1}. Specifically, they effectively inhibited biofilm formation by *B. subtilis* at 100 μg mL^{-1} and 50 μg mL^{-1} for both NPs and by *E. coli*, (ZnO NPs) and *S. aureus* (α-Fe_2O_3-NPs) at 100 μg mL^{-1}. Regarding the anti-biofilm activity of ZnO NPs, it is noteworthy that although zinc plays a crucial role in biofilm development, some research has shown that ZnO NPs can promote biofilm formation in certain bacterial species[122,123] (Fig. S3 and S4 as given in the SI file).

4.6.1 Mechanistic insights of the antibiofilm activity of ZnO and α-Fe_2O_3 NPs. The antibiofilm effectiveness of ZnO and α-Fe_2O_3 NPs may arise from a synergy of physical interactions and biochemical effects that collectively hinder the formation and persistence of biofilms. A key factor in this activity is the production of ROS, including hydroxyl radicals (˙OH), superoxide ions ($O_2^{-\bullet}$), and hydrogen peroxide (H_2O_2). These species are typically generated when the NPs are exposed to aqueous conditions, particularly in the presence of light and oxygen. Once produced, ROS can infiltrate the biofilm's extracellular matrix, leading to oxidative stress within bacterial cells by damaging essential biomolecules such as lipids, proteins, and DNA. This oxidative damage compromises cell integrity and contributes to the breakdown of the biofilm structure.[124] In addition to ROS involvement, disruption of quorum-sensing (QS) pathways may also play an important role. QS is a cell-density-dependent signalling mechanism that controls various bacterial behaviours, including biofilm formation, motility, and virulence. NPs can disrupt chemical signaling, including *N*-acyl homoserine lactones in Gram-negative and autoinducing peptides in Gram-positive bacteria, thereby downregulating genes essential for biofilm formation and stability.[125] By impeding this communication, the coordinated formation and maturation of biofilms are disrupted. Moreover, due to their small size and surface characteristics, these nanoparticles can effectively penetrate the extracellular polymeric substances (EPS) that encapsulate bacterial communities. This enhances direct interaction with bacterial cells, facilitating ROS delivery and promoting structural damage, such as membrane disruption and leakage of intracellular contents. Altogether, the combination of oxidative stress, interference in bacterial

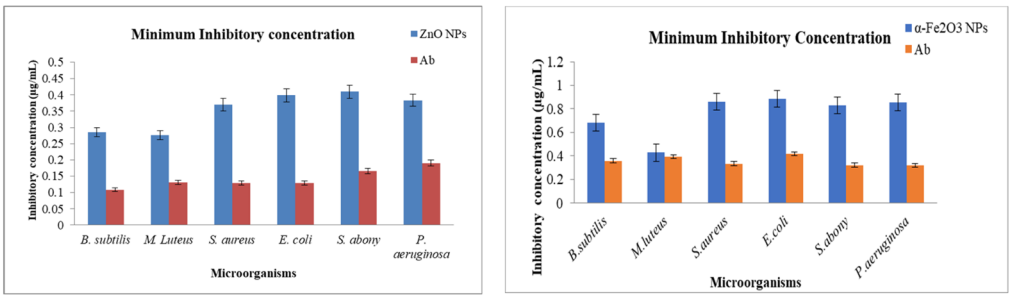

(a) (b)

Fig. 12 MIC graph of (a) ZnO NPs, and (b) α-Fe_2O_3 NPs against selected bacterial strains.

communication systems, and physical disruption of biofilm architecture contributes to the observed reduction in biofilm biomass, as confirmed by microtiter plate-based biofilm assays.[126]

4.7 Antioxidant activity of ZnO and α-Fe_2O_3 NPs

When an antioxidant and the free radical DPPH interact to produce the reduced DPPH-H, the absorbance at 517 nm decreases because the hydrogen content decreases, and the colour changes from purple to yellow as the scavenging of electrons increases, signifying decolourization. NPs may have antioxidant properties because of the electron density transfer from the oxygen atom to the odd electron at the nitrogen atom in DPPH, reducing the strength of the n → π* transition at 517 nm.[127] Using a leaf extract from *Berberis aristata*, Chandra *et al.* produced ZnO NPs and examined their antioxidant properties using the DPPH methodology. The percentage of inhibition for ZnO NPs at 1 and 5 μg mL^{-1} was 32.06 and 61.63%, respectively, while the standard compound, ascorbic acid, had values of 42.16 and 87.76% at 1 and 5 μg mL^{-1}, respectively. ZnO NPs demonstrated less radical scavenging activity than the standard.[128] According to the antioxidant assay results (Table 3), the synthesized ZnO NPs exhibited the highest antioxidant activity (100 μg mL^{-1}) at 517 nm with an antioxidant percentage of 48.63%, while ascorbic acid (positive control) displayed an absorbance of 0.248 at 517 nm with an antioxidant percentage of 73.94% with DPPH as given in Table 5. The choice of the positive control, ascorbic acid, was made on the basis that plant extracts usually have high ascorbic acid content, and it is a well-known antioxidant. Similar observations were made in previous studies as well.[129,130] Likewise, DPPH assay has also been employed to assess the antioxidant potential of different NPs.[131,132] Similarly, the antioxidant assay of the synthesized α-Fe_2O_3 NPs showed antioxidant activity (100 μg mL^{-1}) with a DPPH absorbance of 0.603 at 517 nm and an antioxidant percentage of 36.79% as compared to ascorbic acid (positive control) 70.23% with DPPH, which is not very significant. But it may be enhanced by functionalising these NPs using suitable organic ligands. In one study, Fe_2O_3 NPs were produced using green methods and chemical precipitation. To encapsulate Fe_2O_3 NPs, polyvinylpyrrolidone (PVP) and *Azadirachta indica* extract were used. Fe_2O_3 NPs are found as spheroidal cubic and rhombohedral crystal lattices in the maghemite and hematite phases, respectively, and exhibit ferrimagnetic and antiferromagnetic properties. The antioxidant capability of Fe_2O_3 NPs has been evaluated up to 57% and 90%, respectively, using chemical and green methods.[133] Shah *et al.* studied IONPs functionalized with gallic acid (IONPs@GA). They synthesised three functionalized samples of IONPS with gallic acid (IONP@GA1 IONP@GA2, IONP@GA) and evaluated their antioxidant potential. The most likely explanation for the free radical scavenging is electron transfer from IONP@GA to free radicals at the central nitrogen atom of DPPH.[134] Although both the NPs showed lower antioxidant activity than ascorbic acid, in comparison, ZnO NPs showed greater antioxidant activity than α-Fe_2O_3 NPs as given in Table 7.

4.8 Photodegradation of malachite green dye by ZnO and α-Fe_2O_3 NPs as photocatalysts

ZnO NPs are one of the most extensively studied nanoparticles and are widely recognized as a promising photocatalyst for water purification.[135] ZnO had approximately 79% photodegradation effectiveness against the MG dye after 90 minutes of exposure to visible light. Based on the recorded spectra, it was observed that the intensity of the characteristic band at λ_{max} of 618 nm for the dye decreased over time, indicating a decrease in the dye concentration. The degradation percentage was plotted against time (Fig. 13(a)). The pseudo-first-order kinetic model was used to analyze the degradation rate, and the resultant rate constant value was 5.9×10^{-3} min^{-1}. The linearity of the plot ($R^2 = 0.88$) validated the suitability of the pseudo-first-order model for describing the degradation of MG dye under the given experimental conditions, as shown in Fig. 13(b), while for α-Fe_2O_3, 68% (Fig. 14(a)) dye degradation was found against the MG dye after 90 minutes of exposure to visible light. The pseudo-first-order kinetic model was used to analyse the degradation rate of α-Fe_2O_3 NPs, and the resultant rate constant values were found to be 4.75×10^{-3} min^{-1} (Fig. 14(b)). Hence, it was shown that the photocatalytic efficiency of ZnO NPs was more than that of α-Fe_2O_3 NPs. ZnO NPs obtained from *Hylocereus polyrhizus* peel extract by a green synthesis were confirmed to be pure, spherical, highly crystalline nanoparticles with an average size of 56 nm and a wurtzite hexagonal phase. They exhibited excellent photocatalytic efficiency in degrading methylene blue under sunlight, as validated by UV-vis and LC-MS analyses.[136] Recently, ZnO NPs synthesized using *Allium caliphalum* leaf extract showed particle sizes of 30–72 nm (SEM) and crystallite sizes of 15–24 nm, with bandgap energies ranging from 3.14 to 3.25 eV depending on the pH. At the optimal pH of 8, the NPs exhibited the highest photocatalytic activity, achieving 74% degradation of methyl orange within 140 minutes, attributed to their smaller size, higher crystallinity,

Table 7 Comparative evaluation of the antioxidant activity of ZnO NPs and α-Fe_2O_3 NPs

S. no.	Sample	DPPH (absorbance at 517 nm)	Scavenging percentage (mg mL^{-1})
1	Control	0.952 (±0.021)	—
2	Ascorbic acid	0.219 (±0.014) (ZnO NPs)	78.99% (ZnO NPs)
		0.284 (±0.02) (α-Fe_2O_3 NPs)	70.23% (α-Fe_2O_3 NPs)
3	ZnO NPs	0.489 (±0.042)	48.63%
4	α-Fe_2O_3 NPs	0.603 (±0.04)	36.79%

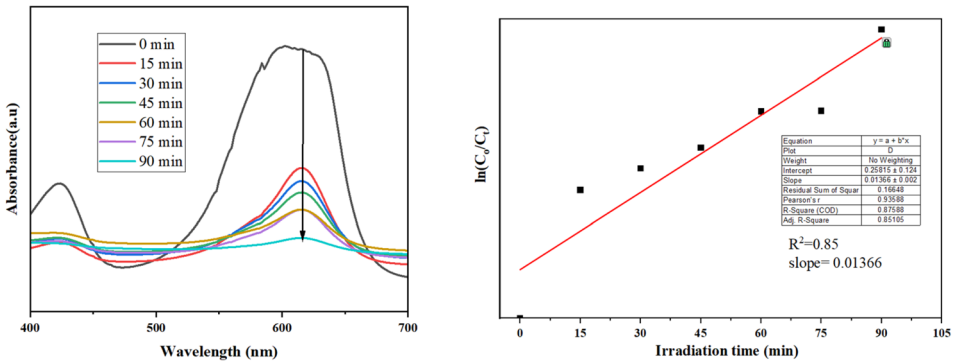

Fig. 13 (a) UV-vis spectrum exhibiting photodegradation of MG dye by ZnO NPs at different times, and (b) pseudo-first-order kinetic plot of $\ln(C_o/C_t)$ *vs.* time.

and favourable bandgap.[137] In another recent study, ZnO NPs synthesized *via* a green route using ginger extract exhibited strong photocatalytic potential. The extract concentration played a key role in tuning their morphology, size, and surface area, which directly influenced their degradation efficiency. ZnO NPs prepared with 5 mL of ginger extract showed the best performance, achieving 44% degradation of methylene blue at pH 4.3 and 83% at pH 5.6 under acidic conditions, highlighting their effectiveness for wastewater treatment applications.[138] Lu *et al.* biosynthesized ZnO NPs using *Codonopsis lanceolata* root extract, where saponins acted as natural capping agents. The Cl–ZnO NPs showed strong photocatalytic efficiency, achieving 90.3% degradation of methylene blue within 40 min under UV irradiation with a rate constant (k) of 0.057. The results highlight the potential of *C. lanceolata* extract in producing cost-effective, eco-friendly ZnO photocatalysts for wastewater treatment.[139] ZnO NPs synthesized using *Phoenix roebelenii* leaf extract were nearly spherical with a crystallite size of ~15.6 nm and a bandgap of 3.24 eV. They exhibited excellent photocatalytic activity, achieving 98% degradation of methylene blue within 105 min under UV irradiation.[140] The photocatalytic activity of some previoussly synthesized ZnO and Fe_2O_3 NPs has been presented in Tables 8 and 9.

It has been found that both visible and ultraviolet light can activate metal oxide nanoparticles (MO NPs) (ZnO NPs, or α-Fe_2O_3), resulting in the formation of electron–hole pairs (e^-/h^+). Due to holes, H_2O molecule in the solution is broken up into $OH^\bullet$ and H^+. Moreover, superoxide radical anions (O_2^-) are generated from dissolved oxygen molecules, and these anions combine with hydrogen ions (H^+) to generate $HO^\bullet$ radicals.[141] These hydroxy radicals degraded the dye as illustrated in Fig. 15. In general, the photocatalytic degradation mechanism of MO involves the steps given in eqn (17)–(20).[142] Moreover, the present findings were also compared with some of the previously reported studies, as given in Table 6.

$$\text{Formation of hole–e pair MO} + h\nu \rightarrow \text{MO} + h^+ + e^- \quad (17)$$

$$\text{Formation of hydroxy radical } h^+ + H_2O \rightarrow OH^\bullet + H^+ \quad (18)$$

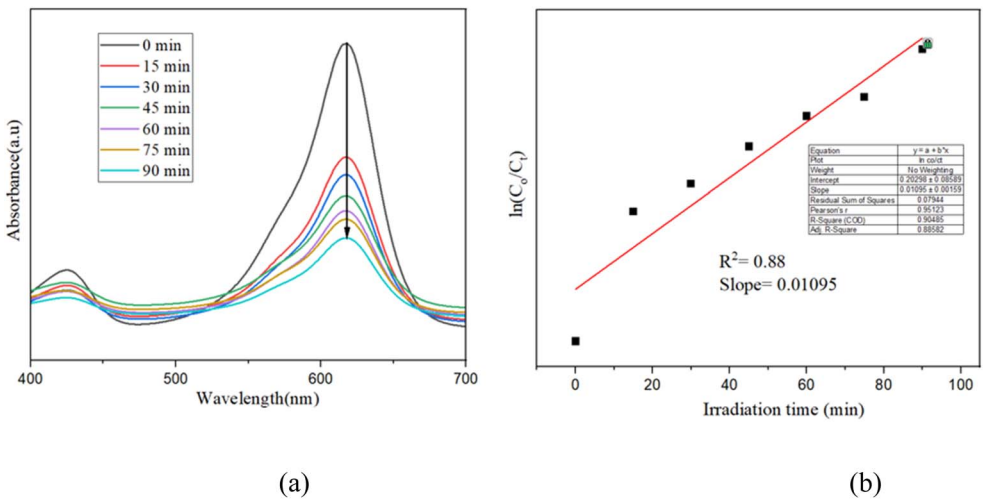

Fig. 14 (a) UV-vis spectrum exhibiting photodegradation of MG dye by Fe_2O_3 NPs at different times, and (b) pseudo-first-order kinetic plot of $\ln(C_o/C_t)$ *vs.* time.

Table 8 ZnO NPs obtained by green synthesis and their photocatalytic activity towards different dyes

S. no.	Plant extract	Dye	Light source	Time (minutes)	Degradation efficiency (%)	Ref.
1	*Gynostemma pentaphyllum*	MG	UV	180	89	144
3	*Spartina alterniflora*	MG	Visible	60	49	145
4	*Nephelium lappaceum* L	MO	UV	120	83	146
5	*Syzygium cumini*	MB	Sunlight	180	91	147
6	*Calotropis procera*	MO	UV	100	81	148
7	*Terminalia chebula*	RHB	UV	300	70	149
8	Eucalyptus leaf	MG	UV	60	90	150
9	***Livistona chinensis***	**MG**	**Visible**	**90**	**79**	**Present study**

Table 9 α-Fe_2O_3 NPs obtained by green synthesis and their photocatalytic activity towards different dyes

S. no.	Plant extract	Dye	Light source	Time (minutes)	Degradation efficiency (%)	Ref.
1	*Mentha pulegium*	MB	UV	120	78	151
2	*Ziziphus jujuba*	MB	Visible	160	92.8	152
3	*Azadirachta indica*	MG	UV	70	92	153
4	*Psidium guajava*	MB	UV	40	93	154
		RHB	UV	40	96	
5	*Moringa stenopetala*	MB	—	180	96	155
6	*Musa acuminata*	CV	Sunlight	150	90.27	156
7	*Achyranthes aspera*	Bromothymol	Sunlight	60	96	157
8	***Livistona chinensis***	**MG**	**Visible**	**90**	**68**	**Present study**

Formation of oxygen radical anion $O_2 + e^- \rightarrow {}^{\bullet}O_2^-$ (19)

Dye degradation ${}^{\bullet}O_2^- + OH^{\bullet} + C_{52}H_{54}N_4O_{12} \rightarrow$
$CO_2 + H_2O$ + mineral acids (malachite green) (20)

4.8.1 LC-MS analysis of MG dye degradation. LC-MS analysis was performed to identify the degradation products of MG dye when treated with ZnO NPs after 45 minutes under visible light irradiation. It is well known from the literature that the hydroxyl radicals generated by ZnO NPs act as highly reactive species, facilitating oxidation of the dye and initiating its breakdown. The proposed degradation mechanism involves hydroxylation, *N*-demethylation, oxidation, deamination, and cleavage of the aromatic rings, consistent with pathways reported by Barapatre *et al.*[158] These reactions lead to the formation of smaller, less toxic molecules, which can ultimately result in complete mineralization.

LC-MS of the standard MG sample showed a dominant peak at *m*/*z* 329.5, corresponding to the intact cation ($C_{23}H_{25}N_2^+$). Upon treatment with ZnO NPs, the intensity of this peak decreased from 75 913 to 45 193 abundance after 45 minutes, which is consistent with the UV UV-visible degradation graph as given in Fig. 13 indicating partial mineralization. New peaks at *m*/*z* 136.1, 195.2, and 274.5 corresponded to demethylated products, hydroxylated/oxidized intermediates, and low-mass aromatic fragments. Recently, Nikita *et al.* also studied the degradation of MG dye by using La-doped ZnO NPs by using LC-MS analysis, and they also proposed the degradation of the dye through *N*-demethylation, oxidation, and deamination mechanisms.[159] The chromatograms of the standard MG dye and that treated with ZnO NPs have been given as SI Fig. S5 and S6. These findings suggest that ZnO NPs degrade MG through *N*-demethylation, oxidative hydroxylation, and aromatic ring cleavage, ultimately leading to dye decomposition.

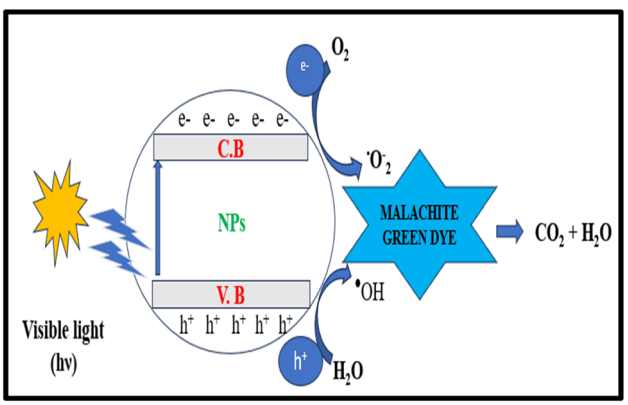

Fig. 15 Probable mechanism for MG dye degradation by NPs.[143]

4.9 Molecular docking

It's important to understand how the NPs interact with the proteins of interest by binding to them. Molecular docking analyses the protein–ligand complex's binding affinity as well as the type of interactions, such as weak van der Waals, covalent, and ionic.[160] The molecular docking analysis demonstrated that ZnO NPs interacted with all three target quorum-sensing

proteins, as indicated by low binding energies and high inhibition constants (K_i). *P. aeruginosa* may attack people suffering from AIDS, cancer, cystic fibrosis *etc. P. aeruginosa* is a nosocomial bacterium that affects patients with cystic fibrosis, lung diseases, burns, open fractures, *etc.* The pathogen is usually resistant to multiple antibiotics, leading to persistent infection.[161] Recent studies have demonstrated that quorum sensing (QS), a bacterial cell-to-cell communication mechanism, plays a significant role in regulating the expression of virulence genes in *P. aeruginosa.* The bacterium develops biofilms by using a quorum-sensing mechanism. The swarming motility protein BswR and the quorum-sensing proteins LasI and LasR of the Las system are essential for the biofilm-mediated antibiotic resistance phenomena.[162] Previously, it has been found that LasR protein may act as a dimer and bind to the promoter DNA with the help of an autoinducer ligand.[163] Other than that, several bacterial strains have utilized a cell density-dependent mechanism or quorum sensing (QS) to express various genes.[164] Las is one of the two main QS systems of *Pseudomonas aeruginosa*.[165]

Against the LasR protein of *Pseudomonas aeruginosa* (PDB: 4NG2), ZnO NPs exhibited a binding energy of −3.35 kcal mol^{-1}, a K_i of 3500.9 μM, and formed six hydrogen bonds with TYR 153 (1.34 Å, 3.19 Å), LYS 325 (2.71 Å), and HIS 227 (2.08 Å, 2.37 Å, 1.93 Å) along with interactions with SER 151. With Fe_2O_3 NPs, the LasR protein interacted by forming four hydrogen bonds with residues SER28, GLY54, ARG29, ILE52, ARG61, and ASP65, as well as a binding energy of −9.89 kcal mol^{-1} and a K_i of 0.05621 μM. Inhibiting the LasI protein is a desirable therapeutic target because LasI (1RO5) is an acyl-homoserine lactone synthase that generates the QS signal, which positively regulates *P. aeruginosa* virulence factors.[166] The interaction of the ZnO NPs with the LasI protein showed a slightly better binding energy of −3.86 kcal mol^{-1} and a K_i of 1480.2 μM, and formed six hydrogen bonds with residues GLU 133 (1.87 Å), GLY 31 (2.99 Å), SER 33 (1.81 Å, 2.7 Å, 3.25 Å), SER 131 (2.91 Å) and ARG104, and also interacts with LYS 34. *S. aureus* exhibits complex pathogenicity involving the expression of different virulence factors. Adhesins on the surface of proteins are formed during their exponential growth phase, and the post-exponential phase leads to enhanced toxin production and the production of enzymes, leading to tissue destruction.[167]

α-Fe_2O_3 NPs exhibited the strongest interaction with the LasI protein of *P. aeruginosa*, showing binding energy of −10.33 kcal mol^{-1}, an inhibition constant (K_i) of 0.02674 μM, and three hydrogen bonds with residues ARG104, PHE105, ALA106, PHE117, ARG30, THR144, VAL143, and TRP33. Another widespread organism in swollen skin and soft tissue infections (SSTIs) is *S. aureus*. The accumulation of signal molecules and the expression of virulence factors, such as cell wall-associated proteins, are facilitated by the accessory gene regulator (Agr) QS pathway. The spread of biofilm is facilitated by increased Agr activity.[168] However, when Agr expression increases, more virulence factors are produced. Agr mediates phase transitions by suppressing surface protein expression and encouraging the release of extracellular toxins.[169] RNAII and RNAIII are two different transcripts that constitute the Agr locus. Genes encoded by RNAII include agrDBCA. When AgrA binds to specific direct repeats in the intergenic region between the RNAII and RNAIII promoters, the transcription of Agr can be regulated.[170] When RNAIII, the Agr effector molecule, is activated, many surface-associated proteins are repressed, whereas exoprotein gene transcription and, to a lesser extent, translation are promoted. For the AgrA protein of *Staphylococcus aureus* (PDB: 4 G4K), ZnO exhibited a binding energy of −3.75 kcal mol^{-1}, a K_i of 1782.2 μM, and formed five hydrogen bonds with PHE 105 (1.90 Å, 2.70 Å, 1.74 Å), ARG 104 (3.61 Å), MET 79 (2.16 Å), alongside interactions with ASP 44. For α-Fe_2O_3 NPs with the AgrA protein of *S. aureus*, the binding energy of −8.05 kcal mol^{-1}, a K_i of 1.2552 μM, and six hydrogen bonds involving HIS174, GLN179, GLU226, TYR153, VAL154, ASP158, ASP176, ARG178, ASN177, TUR229, and HIS200 were obtained. With the autoinducer protein-2 (AI-2) of *E. coli*, a binding energy of −6.77 kcal mol^{-1} was obtained, with a K_i of 10.89 μM, and three hydrogen bonds with residues ILE186, GLN173, PRO169, ASN48, and VAL45. AI-2 is an active methyl cycle metabolic byproduct of *S*-adenosylhomocysteine detoxification. It is known as the broad-spectrum interspecies QS molecule.[171] It can alter gene expression, trigger a chemotactic response, or activate phages in several bacterial species. These findings highlight the potential of α-Fe_2O_3 NPs to modulate quorum sensing, particularly in *P. aeruginosa*.

The docking results indicate that α-Fe_2O_3 NPs had a high binding affinity toward quorum-sensing proteins, particularly LasI and LasR of *P. aeruginosa*. These strong interactions suggest that the NPs could inhibit quorum sensing and associated pathogenic behaviours such as biofilm formation and virulence factor production. The moderate interaction with AgrA protein highlights the variability in α-Fe_2O_3 NPs' efficacy against different bacterial signalling pathways. These differences may be attributed to variations in active site geometry and electrostatic properties of the target proteins. The findings suggest that α-Fe_2O_3 NPs could serve as promising agents to target quorum sensing in bacterial pathogens. However, for ZnO NPs, the affinity towards quorum-sensing proteins is moderate under the tested conditions, suggesting that further

Table 10 Binding energy of ZnO NPs with target proteins

Target protein	Key interaction	Binding energy (kcal mol^{-1})	K_i (μM)	No. of H-bonds
LasR	TYR153, LYS325, HIS227, SER151	−3.35	3500.9	1
LasI	GLU133, GLY31, SER33, SER131, ARG104, LYS34	−3.86	1480.2	0
AgrA	PHE105, ARG104, MET79, ASP44	−3.75	1782.2	1

Table 11 Binding energy of α-Fe_2O_3 NPs with target proteins

Target protein	Key interaction	Binding energy (kcal mol^{-1})	K_i (μM)	No. of H-bonds
LasR	SER28, GLY54, ARG29, ILE52, ARG61, ASP65	−9.89	0.05621	4
LasI	ARG104, PHE105, ALA106, PHE117, ARG30, THR144, VAL143, TRP33	−10.33	0.02674	3
AgrA	HIS174, GLN179, GLU226, TYR153, VAL154, ASP158, ASP176, ARG178, ASN177, TUR229, HIS200	−8.05	1.2552	6

modification or functionalization may improve the binding affinity and efficacy as a quorum-sensing modulator. Docking poses are shown in Fig. S7–S12 in the SI file, and Table 10 and 11 summarizes the docking results.

5. Conclusion

This study presents the green synthesis of ZnO and α-Fe_2O_3 NPs using *Livistona chinensis* leaf extract, an eco-friendly and cost-effective approach. The synthesized ZnO NPs (average size ~25.4 nm) exhibited triangular morphology, while α-Fe_2O_3 NPs (~12.4 nm) were spherical. Both types of nanoparticles showed significant antibacterial activity, with ZnO NPs inhibiting *M. luteus* and *S. abony* (ZOI ~15 mm at 50 μg mL^{-1}) and α-Fe_2O_3 NPs effectively targeting *B. subtilis*, *S. aureus*, and *E. coli* (ZOI ~19–21 mm at 100 μg mL^{-1}). Both NPs also demonstrated notable antibiofilm and moderate antioxidant activities, scavenging 48.63% and 36.79% of DPPH radicals, respectively. ZnO NPs showed superior photocatalytic efficiency, degrading 79% of malachite green dye under visible light within 90 minutes, compared to 68% for α-Fe_2O_3 NPs. LC-MS analysis confirmed the decrease of the main MG peak (m/z 329.5) and formation of intermediates at m/z 274.5, 195.2, and 136.1, indicating *N*-demethylation, oxidation, and deamination. However, the study is limited by the lack of advanced microscopy techniques (*e.g.*, FESEM of bacterial morphology) and magnetic or anticancer evaluations, due to resource constraints. Future studies will aim to address these gaps and explore the functionalization of these nanoparticles for enhanced biological performance. Overall, the findings highlight the promising multifunctional applications of these biogenic NPs in environmental and biomedical fields. Future work will focus on exploring magnetic properties, anticancer potential, and functionalization strategies to enhance biological activities.

Author contributions

Ekhlakh Veg – investigation, formal analysis, interpretation, writing – original and final draft; Azam Raza – characterization and interpretation; Smita Rai – antibacterial activity evaluation; Swati Sharma – antibacterial activity evaluation; Pratibha Bansal – photocatalytic activity; Nidhi Mishra – molecular docking; Riya Gupta – photocatalytic activity; Shivam Mishra – molecular docking; Seema Joshi – co-supervision and proofreading; Abdul Rahman Khan – resources; Tahmeena Khan – conceptualization, supervision, writing – final draft and proof-reading.

Conflicts of interest

The authors have no competing interests.

Data availability

All the data generated during the study have been included in the manuscript.

Supplementary information is available. See DOI: **https://doi.org/10.1039/d5su00349k**.

Acknowledgements

The authors are thankful to the R&D Cell, Integral University, for providing the Manuscript Communication Number (IU/R&D/2025-MCN0003295). They are also thankful to the Central Instrumentation Facility, Integral University, for the necessary support.

References

1 R. A. Bapat, C. P. Joshi, P. Bapat, T. V. Chaubal, R. Pandurangappa, N. Jnanendrappa, B. Gorain, S. Khurana and P. Kesharwani, *Drug Discovery Today*, 2018, **24**, 85–98, DOI: **10.1016/j.drudis.2018.08.012**.
2 S. Jabeen, E. Veg, S. Bala and T. Khan, *Eng. Proc.*, 2024, **6**, 7008, DOI: **10.3390/engproc2024067008**.
3 M. P. Nikolova and M. S. Chavali, *Biomimetics*, 2020, **5**, 27, DOI: **10.3390/biomimetics5020027**.
4 E. Veg, K. Hashmi, S. Raza, S. Joshi, A. R. Khan and T. Khan, *Chem. Biodiversity*, 2024, **22**, e202401581, DOI: **10.1002/cbdv.202401581**.
5 N. Satya, K. Hashmi, S. Gupta, N. Singh and T. Khan, *Russ. J. Gen. Chem.*, 2023, **93**, 635–665, DOI: **10.1134/S1070363223030209**.
6 P. Slepička, N. S. Kasálková, J. Siegel, Z. Kolská and V. Švorčík, *Materials*, 2019, **13**, 1, DOI: **10.3390/ma13010001**.
7 E. Veg, S. Joshi and T. Khan, *Eng. Proc.*, 2024, **13**, 46, DOI: **10.3390/engproc2024067046**.
8 D. Gupta, A. Boora, A. Thakur and T. K. Gupta, *Environ. Res.*, 2023, **231**, 116316, DOI: **10.1016/j.envres.2023.116316**.
9 L. Chen, I. Batjikh, J. Hurh, Y. Han, Y. Huo, H. Ali, J. F. Li, E. J. Rupa, J. C. Ahn, R. Mathiyalagan and D. C. Yang, *Optik*, 2019, **184**, 324–329, DOI: **10.1016/j.ijleo.2019.03.051**.

10 M. D. Jayappa, C. K. Ramaiah, M. A. P. Kumar, D. Suresh, A. Prabhu, R. P. Devasya and S. Sheikh, *Appl. Nanosci.*, 2020, **10**, 3057–3074, DOI: 10.1007/s13204-020-01382-2.
11 W. Maret, *BioMetals*, 2011, **24**, 411–418, DOI: 10.1007/s10534-010-9406-1.
12 Y. Wang, J. Cao, S. Wang, X. Guo, J. Zhang, H. Xia and S. Wu, *J. Phys. Chem. C*, 2008, **112**, 17804–17808, DOI: 10.1021/jp806430f.
13 G. Neri, A. Bonavita, S. Galvagno, P. Siciliano and S. Capone, *Sens. Actuators, B*, 2002, **82**, 40–47, DOI: 10.1016/S0925-4005(01)00987-X.
14 Z. H. Jing and S. H. Wu, *Mater. Chem. Phys.*, 2005, **92**, 600–603, DOI: 10.1016/j.matchemphys.2005.02.005.
15 K. A. Nxumalo, J. O. Adeyemi, T. B. Leta, *et al.*, *Sci. Rep.*, 2024, **14**, 18071, DOI: 10.1038/s41598-024-68979.
16 S. Naz, M. Islam, S. Tabassum, N. F. Fernandes, E. J. C. de Blanco and M. Zia, *J. Mol. Struct.*, 2019, **1185**, 1–7, DOI: 10.1016/j.molstruc.2019.02.088.
17 J. O. Adeyemi, D. C. Onwudiwe and A. O. Oyedeji, *Molecules*, 2022, **27**, 3206, DOI: 10.3390/molecules27103206.
18 S. V. Gudkov, D. E. Burmistrov, D. A. Serov, M. B. Rebezov, A. A. Semenova and A. B. Lisitsyn, *Front. Phys.*, 2021, **9**, 641481, DOI: 10.3389/fphy.2021.641481.
19 M. Aminuzzaman, *et al.*, *Bull. Mater. Sci.*, 2018, **41**, 50, DOI: 10.1007/s12034-018-1568-4.
20 M. Ramar, *et al.*, *J. Photochem. Photobiol., B*, 2019, **199**, 111650, DOI: 10.1016/j.jphotobiol.2019.111650.
21 M. Ashaduzzaman, M. M. A. Muhit, S. C. Dey, M. M. Rahaman, H. N. M. Hasan, N. Mustary, M. K. Hossain and M. K. Das, *Sci. Rep.*, 2025, **15**(1), DOI: 10.1038/s41598-025-14193-8.
22 B. L. Da Silva, B. L. Caetano, B. G. Chiari-Andréo, R. C. L. R. Pietro and L. A. Chiavacci, *Colloids Surf., B*, 2019, **177**, 440–447, DOI: 10.1016/j.colsurfb.2019.02.013.
23 S. K. Urge, S. T. Dibaba and A. B. Gemta, *J. Nanomater.*, 2023, **2023**, 7036247, DOI: 10.1155/2023/7036247.
24 G. K. Prashanth, A. S. Giresha, H. S. Lalithamba, M. Aman, S. Rao, K. N. Ravindra, M. Gadewar, N. P. Bhagya, M. M. Swamy and V. Chaturvedi, *Inorg. Chem. Commun.*, 2024, 113592, DOI: 10.1016/j.inoche.2024.113592.
25 D. Das, B. C. Nath, P. Phukon, A. Kalita and S. K. Dolui, *Colloids Surf., B*, 2013, **111**, 556–560, DOI: 10.1016/j.colsurfb.2013.06.041.
26 S. Sharma and A. Kaur, *Indian J. Sci. Technol.*, 2018, **11**, 1–21, DOI: 10.17485/ijst/2018/v11i12/120847.
27 P. V. Kamat, *J. Phys. Chem. Lett.*, 2012, **3**, 663–672, DOI: 10.1021/jz201629p.
28 H. Zhang, R. Zong, J. Zhao and Y. Zhu, *Environ. Sci. Technol.*, 2008, **42**, 3803–3807, DOI: 10.1021/es703037x.
29 M. F. Elkady and H. S. Hassan, *Polymers*, 2021, **13**, 2033, DOI: 10.3390/polym13132033.
30 B. S. Giri, R. K. Sonwani, S. Varjani, D. Chaurasia, T. Varadavenkatesan, P. Chaturvedi, S. Yadav, V. Katiyar, R. S. Singh and A. Pandey, *Chemosphere*, 2021, **287**, 132282, DOI: 10.1016/j.chemosphere.2021.132282.
31 S. Ghaffar, A. Abbas, M. Naeem-Ul-Hassan, N. Assad, M. Sher, S. Ullah, H. A. Alhazmi, A. Najmi, K. Zoghebi, M. A. Bratty, A. Hanbashi, H. A. Makeen and H. M. A. Amin, *Antioxidants*, 2023, **12**, 1201, DOI: 10.3390/antiox12061201.
32 J. K. Park, E. J. Rupa, M. H. Arif, J. F. Li, G. Anandapadmanaban, J. P. Kang, M. Kim, J. C. Ahn, R. Akter, D. C. Yang and S. C. Kang, *Optik*, 2021, **239**, 166249, DOI: 10.1016/j.ijleo.2020.166249.
33 S. N. A. M. Sukri, E. D. M. Isa and K. Shameli, *IOP Conf. Ser. Mater. Sci. Eng.*, 2020, **808**, 012034, DOI: 10.1088/1757-899X/808/1/012034.
34 A. Bhuin, S. Udayakumar, J. Gopalarethinam, D. Mukherjee, K. Girigoswami, C. Ponraj and S. Sarkar, *Sci. Rep.*, 2024, **14**, 10406, DOI: 10.1038/s41598-024-59842-6.
35 A. Girigoswami, B. Deepika, S. Udayakumar, G. Janani, D. J. Mercy and K. Girigoswami, *BMC Pharmacol. Toxicol.*, 2024, **25**, 101, DOI: 10.1186/s40360-024-00830-x.
36 D. Khadka, P. Gautam, R. Dahal, M. D. Ashie, H. Paudyal, K. N. Ghimire, B. Pant, B. R. Poudel, B. P. Bastakoti and M. R. Pokhrel, *Catalysts*, 2024, **14**, 751, DOI: 10.3390/catal14110751.
37 M. Mishra and D.-M. Chun, *Appl. Catal., A*, 2015, **498**, 126–141, DOI: 10.1016/j.apcata.2015.03.023.
38 X. Wen, S. Wang, Y. Ding, Z. L. Wang and S. Yang, *J. Phys. Chem. B*, 2004, **109**, 215–220, DOI: 10.1021/jp0461448.
39 S. Majidi, F. Z. Sehrig, S. M. Farkhani, M. S. Goloujeh and A. Akbarzadeh, *Artif. Cells, Nanomed. Biotechnol.*, 2014, **44**, 722–734, DOI: 10.3109/21691401.2014.982802.
40 A. T. Bell, *Science*, 2003, **299**, 1688–1691, DOI: 10.1126/science.1083671.
41 Y. Wang, J. Cao, S. Wang, X. Guo, J. Zhang, H. Xia, S. Zhang and S. Wu, *J. Phys. Chem. C*, 2008, **112**, 17804–17808, DOI: 10.1021/jp806430f.
42 G. Neri, A. Bonavita, S. Galvagno, P. Siciliano and S. Capone, *Sens. Actuators, B*, 2002, **82**, 40–47, DOI: 10.1016/S0925-4005(01)00987-X.
43 Z. H. Jing and S. H. Wu, *Mater. Chem. Phys.*, 2005, **92**, 600–603, DOI: 10.1016/j.matchemphys.2005.02.005.
44 K. K. Kefeni, T. A. M. Msagati, T. T. I. Nkambule and B. B. Mamba, *J. Environ. Chem. Eng.*, 2018, **6**, 1865–1874, DOI: 10.1016/j.jece.2018.02.037.
45 S. Naz, M. Islam, S. Tabassum, N. F. Fernandes, E. J. C. de Blanco and M. Zia, *J. Mol. Struct.*, 2019, **1185**, 1–7, DOI: 10.1016/j.molstruc.2019.02.088.
46 H. R. El-Seedi, M. S. Omara, A. H. Omar, M. M. Elakshar, Y. M. Shoukhba, H. Duman and S. A. Khalifa, *Bioengineering*, 2024, **11**, 1095, DOI: 10.3390/bioengineering11111095.
47 L. Chen, I. Batjikh, J. Hurh, Y. Han, Y. Huo, H. Ali, J. F. Li, E. J. Rupa, J. C. Ahn, R. Mathiyalagan and D. C. Yang, *Optik*, 2019, **184**, 324–329, DOI: 10.1016/j.ijleo.2019.03.051.
48 M. D. Jayappa, C. K. Ramaiah, M. A. P. Kumar, D. Suresh, A. Prabhu, R. P. Devasya and S. Sheikh, *Appl. Nanosci.*, 2020, **10**, 3057–3074, DOI: 10.1007/s13204-020-01382-2.
49 S. Jabeen, V. U. Siddiqui, S. Bala, N. Mishra, A. Mishra, R. Lawrence, P. Bansal, A. R. Khan and T. Khan, *ACS Omega*, 2024, **9**, 30190–30204, DOI: 10.1021/acsomega.3c10179.

50 H. J. Fatih, M. Ashengroph, A. Sharifi and M. M. Zorab, *BMC Microbiol.*, 2024, **24**, 3699, DOI: 10.1186/s12866-024-03699-2.
51 M. S. Aida, N. Alonizan, B. Zarrad and M. Hjiri, *Journal of Taibah University for Science*, 2023, **17**, 2221827, DOI: 10.1080/16583655.2023.2221827.
52 M. Bashir, S. Ali and M. A. Farrukh, *J. Korean Phys. Soc.*, 2020, **76**, 848–854, DOI: 10.3938/jkps.76.848.
53 S. J. Rojas, Livistona Chinensis (Chinese Fan Palm), *CABI Compendium*, CABI Int, 2017, DOI: 10.1079/cabicompendium.31059.
54 S. Li, S. Luo, H. Chen, Y. Zheng, L. Lin, H. Yao and X. Lin, *Drug Des., Dev. Ther.*, 2019, **8**(13), 1555–1566.
55 X. Cheng, F. Zhong, K. He, S. Sun, H. Chen and J. Zhou, *Oncol. Lett.*, 2016, **12**, 3739–3748, DOI: 10.3892/ol.2016.5178.
56 M. Mohammed and M. Fouad, *J. Adv. Biomedical Pharm. Sci.*, 2022, **5**, 113–150, DOI: 10.21608/jabps.2022.126338.1149.
57 W.-C. Huang, Y.-L. Leu and J.-S. Yu, in *Cancer and Treatment with Seeds of Chinese Fan Palm (Livistona Chinensis R. Brown)*, Elsevier eBooks, 2011, pp. 325–331, DOI: 10.1016/b978-0-12-375688-6.10039-8.
58 E. Veg, A. Raza, S. Rai, S. Sharma, A. Pandey, M. I. Ahmad, S. Jabeena, S. Joshi and T. Khan, *Chem. Biodiversity*, 2024, **22**, e202401596, DOI: 10.1002/cbdv.202401596.
59 E. Veg, A. Raza, P. Bansal, S. Rai, S. Sharma, S. Dwivedi, *et al.*, *Surf. Interfaces*, 2025, **54**, 107271, DOI: 10.1016/j.surfin.2025.107271.
60 S. T. Karam and A. F. Abdulrahman, *Photonics*, 2022, **9**, 594, DOI: 10.3390/photonics9080594.
61 S. S. Alias, A. B. Ismail and A. A. Mohamad, *J. Alloys Compd.*, 2010, **499**, 231–237, DOI: 10.1016/j.jallcom.2010.03.174.
62 F. Islam, S. Shohag, M. J. Uddin, M. R. Islam, M. H. Nafady, A. Akter, S. Mitra, A. Roy, T. B. Emran and S. Cavalu, *Mater*, 2022, **15**, 2160, DOI: 10.3390/ma15062160.
63 A. A. Barzinjy and H. H. Azeez, *SN Appl. Sci.*, 2020, **2**, 1–14, DOI: 10.1007/s42452-020-2813-1.
64 M. Mohammadzaheri, S. Jamehbozorgi, M. D. Ganji, M. Rezvani and Z. Javanshir, *Phys. Chem. Chem. Phys.*, 2023, **25**, 21492–21508, DOI: 10.1039/d3cp01490h.
65 E. Veg, A. Raza, P. Bansal, S. Rai, S. Sharma, R. Gupta, *et al.*, *Inorg. Chem. Commun.*, 2025, **163**, 115265, DOI: 10.1016/j.inoche.2025.115265.
66 K. Biswas, D. J. Mercy, S. Udayakumar, A. Girigoswami and K. Girigoswami, *BioNanoScience*, 2025, **15**, 2, DOI: 10.1007/s12668-025-01866-x.
67 R. B. Fulindi, J. D. Rodrigues, T. W. L. Barbosa, A. D. G. Garcia, F. De Almeida La Porta, S. Pratavieira, L. A. Chiavacci, J. P. Araújo Junior, P. I. Da Costa and L. R. Martinez, *Microbiol. Spectr.*, 2023, **11**, e04831, DOI: 10.1128/spectrum.04831-22.
68 S. A. Khan, S. Shahid, B. Shahid, U. Fatima and S. A. Abbasi, *Biomolecules*, 2020, **10**, 785, DOI: 10.3390/biom10050785.
69 P. C. Nagajyothi, M. Pandurangan, D. H. Kim, T. V. M. Sreekanth and J. Shim, *J. Cluster Sci.*, 2016, **28**, 245–257, DOI: 10.1007/s10876-016-1082-z.
70 P. C. Nagajyothi, M. Pandurangan, D. H. Kim, T. V. M. Sreekanth and J. Shim, *J. Cluster Sci.*, 2016, **28**, 245–257, DOI: 10.1007/s10876-016-1082-z.
71 V. Srivastava, D. Gusain and Y. C. Sharma, *Ceram. Int.*, 2013, **39**, 9803–9808, DOI: 10.1016/j.ceramint.2013.04.110.
72 B. Kumar, K. Smita, L. Cumbal and A. Debut, *J. Saudi Chem. Soc.*, 2014, **18**, 364–369, DOI: 10.1016/j.jscs.2014.01.003.
73 J. Das and P. Velusamy, *Mater. Res. Bull.*, 2013, **48**, 4531–4537, DOI: 10.1016/j.materresbull.2013.07.049.
74 G. P. Rosa, A. M. L. Seca, M. D. C. Barreto, A. M. S. Silva and D. C. G. A. Pinto, *Appl. Sci.*, 2019, **9**, 2846, DOI: 10.3390/app9142846.
75 L. M. Verma, A. Kumar, A. Kumar, G. Singh, U. Singh, S. Chaudhary and S. Sharma, *Sci. Rep.*, 2024, **14**, 4074, DOI: 10.1038/s41598-024-53682-0.
76 A. Raza, M. Shoeb, F. Mashkoor, S. Rahaman, M. Mobin, C. Jeong, M. Y. Ansari and A. Ahmad, *Mater. Chem. Phys.*, 2022, **286**, 126173, DOI: 10.1016/j.matchemphys.2022.126173.
77 D. E. Fouad, C. Zhang, H. El-Didamony, L. Yingnan, T. D. Mekuria and A. H. Shah, *Results Phys.*, 2019, **12**, 1253–1261, DOI: 10.1016/j.rinp.2019.01.005.
78 M. Alagiri and S. B. A. Hamid, *J. Mater. Sci.: Mater. Electron.*, 2014, **25**, 3572–3577, DOI: 10.1007/s10854-014-2058-0.
79 H. Sridevi, M. R. Bhat, P. S. Kumar, N. M. Kumar and R. Selvaraj, *Appl. Nanosci.*, 2023, **13**, 5605–5613, DOI: 10.1007/s13204-023-02780-y.
80 P. Balu, I. V. Asharani and D. Thirumalai, *J. Mater. Sci.: Mater. Electron.*, 2020, **31**, 10669–10676, DOI: 10.1007/s10854-020-03616-z.
81 S. Venkatesan, S. Suresh, J. Arumugam, P. Ramu, N. Pugazhenthiran, R. Jothilakshmi and K. M. Prabu, *Results Chem.*, 2024, **7**, 101315, DOI: 10.1016/j.rechem.2024.101315.
82 S. G. Pandya, J. P. Corbett, W. M. Jadwisienczak and M. E. Kordesch, *Phys. E*, 2015, **79**, 98–102, DOI: 10.1016/j.physe.2015.12.013.
83 Y. Tang, H. Zhou, K. Zhang, J. Ding, T. Fan and D. Zhang, *Chem. Eng. J.*, 2014, **262**, 260–267, DOI: 10.1016/j.cej.2014.09.095.
84 J. Jana, M. Ganguly and T. Pal, *RSC Adv.*, 2016, **6**, 86174–86211, DOI: 10.1039/C6RA14173K.
85 J. Ye, B. Li, M. Li, Y. Zheng, S. Wu and Y. Han, *Acta Biomater.*, 2020, **107**, 313–324, DOI: 10.1016/j.actbio.2020.02.036.
86 S. Khan, S. Mansoor, Z. Rafi, B. Kumari, A. Shoaib, M. Saeed, S. Alshehri, M. M. Ghoneim, M. Rahamathulla, U. Hani and F. Shakeel, *J. Mol. Liq.*, 2021, **348**, 118008, DOI: 10.1016/j.molliq.2021.118008.
87 H. Udayagiri, S. S. Sana, L. K. Dogiparthi, R. Vadde, R. S. Varma, J. R. Koduru, G. S. Ghodake, A. R. Somala, V. K. N. Boya, S.-C. Kim and R. R. Karri, *Sci. Rep.*, 2024, **14**, 16321, DOI: 10.1038/s41598-024-69044-9.
88 N. Babayevska, Ł. Przysiecka, I. Iatsunskyi, G. Nowaczyk, M. Jarek, E. Janiszewska and S. Jurga, *Sci. Rep.*, 2022, **12**, 8148, DOI: 10.1038/s41598-022-12134-3.

89 D. Mutukwa, R. T. Taziwa, S. M. Tichapondwa and L. Khotseng, *Int. J. Mol. Sci.*, 2024, **25**, 11621, DOI: 10.3390/ijms252111621.
90 B. H. Shnawa, P. J. Jalil, A. Al-Ezzi, R. M. Mhamedsharif, D. A. Mohammed, D. M. Biro and M. H. Ahmed, *J. Environ. Sci. Health, Part C*, 2023, **42**, 93–108, DOI: 10.1080/26896583.2023.2293443.
91 A. K. Tiwari, S. Jha, S. K. Tripathi, R. Shukla, R. R. Awasthi, A. K. Bhardwaj, A. K. Singh and A. Dikshit, *SN Appl. Sci.*, 2024, **6**, 677, DOI: 10.1007/s42452-024-06049-z.
92 J. Yoonus, R. Resmi and B. Beena, *Mater. Today Proc.*, 2021, **46**, 2969–2974, DOI: 10.1016/j.matpr.2020.12.426.
93 V. Selvanathan, M. Aminuzzaman, L. X. Tan, Y. F. Win, E. S. G. Cheah, M. H. Heng and M. D. Aktharuzzaman, *J. Mater. Res. Technol.*, 2022, **20**, 2931–2941, DOI: 10.1016/j.jmrt.2022.08.028.
94 K. S. Siddiqi, A. U. Rahman, N. Tajuddin and A. Husen, *Nanoscale Res. Lett.*, 2018, **13**, 141, DOI: 10.1186/s11671-018-2532-3.
95 Y. Jiang, L. Zhang, D. Wen and Y. Ding, *Mater. Sci. Eng., C*, 2016, **69**, 1361–1366, DOI: 10.1016/j.msec.2016.08.044.
96 S. Vihodceva, A. Šutka, M. Sihtmäe, M. Rosenberg, M. Otsus, I. Kurvet, K. Smits, L. Bikse, A. Kahru and K. Kasemets, *Nanomaterials*, 2021, **11**, 652, DOI: 10.3390/nano11030652.
97 E. N. Hammad, S. S. Salem, A. A. Mohamed and W. El-Dougdoug, *Appl. Biochem. Biotechnol.*, 2022, **194**, 6053–6067, DOI: 10.1007/s12010-022-04105-1.
98 J. N. Vranish, M. G. Ancona, E. Oh, K. Susumu, G. L. Aragonés, J. C. Breger, S. A. Walper and I. L. Medintz, *ACS Nano*, 2018, **12**, 7911–7926, DOI: 10.1021/acsnano.8b02334.
99 A. Gole, C. Dash, V. Ramakrishnan, S. R. Sainkar, A. B. Mandale, M. Rao and M. Sastry, *Langmuir*, 2001, **17**, 1674–1679, DOI: 10.1021/la001164w.
100 L. M. Armijo, S. J. Wawrzyniec, M. Kopciuch, Y. I. Brandt, A. C. Rivera, N. J. Withers, N. C. Cook, D. L. Huber, T. C. Monson, H. D. C. Smyth and M. Osiński, *J. Nanobiotechnol.*, 2020, **18**, 10, DOI: 10.1186/s12951-020-0588-6.
101 Y. Li, D. Yang, S. Wang, C. Li, B. Xue, L. Yang, Z. Shen, M. Jin, J. Wang and Z. Qiu, *Molecules*, 2018, **23**, 606, DOI: 10.3390/molecules23030606.
102 J. Zúñiga-Miranda, J. Guerra, A. Mueller, A. Mayorga-Ramos, S. E. Carrera-Pacheco, C. Barba-Ostria, J. Heredia-Moya and L. P. Guamán, *Nanomaterials*, 2023, **13**, 2919, DOI: 10.3390/nano13222919.
103 M. Bhushan, Y. Kumar, L. Periyasamy and A. K. Viswanath, *Appl. Nanosci.*, 2018, **8**, 137–153, DOI: 10.1007/s13204-018-0656-5.
104 M. Arakha, S. Pal, D. Samantarrai, T. K. Panigrahi, B. C. Mallick, K. Pramanik, B. Mallick and S. Jha, *Sci. Rep.*, 2015, **5**, 14813, DOI: 10.1038/srep14813.
105 S. M. Abegunde, E. F. Olasehinde and M. A. Adebayo, *Appl. Biol. Chem.*, 2024, **67**, 50, DOI: 10.1186/s13765-024-00874-5.
106 H. Udayagiri, S. S. Sana, L. K. Dogiparthi, R. Vadde, R. S. Varma, J. R. Koduru and R. R. Karri, *Sci. Rep.*, 2024, **14**, 19714, DOI: 10.1038/s41598-024-64687-4.
107 S. Maher, B. Zamina, M. Riaz, S. Riaz, N. Khalid, M. Imran and S. Parveen, *ACS Omega*, 2023, **8**, 46715–46727, DOI: 10.1021/acsomega.3c05947.
108 K. Bhardwaj, D. S. Dhanjal, A. Sharma, E. Nepovimova, A. Kalia, S. Thakur, *et al.*, *Int. J. Mol. Sci.*, 2020, **21**, 9028, DOI: 10.3390/ijms21239028.
109 A. Raj and R. Lawerence, *Nutrition*, 2018, **11**, 1339–1348.
110 M. F. Islam, M. A. S. Miah, A. O. Huq, A. K. Saha, Z. J. Mou, M. M. H. Mondol and M. N. I. Bhuiyan, *Heliyon*, 2024, **10**, e39255, DOI: 10.1016/j.heliyon.2024.e39255.
111 M. Afzal, S. Ullah, N. Assad, M. Naeem-ul-Hassan, M. Kanwal, B. Mubashar, *et al.*, *Green Process. Synth.*, 2024, **13**, 20240038, DOI: 10.1515/gps-2024-0038.
112 M. C. Ogwuegbu, O. C. Olatunde, T. M. Pfukwa, D. M. Mthiyane, O. A. Fawole and D. C. Onwudiwe, *Discov. Appl. Sci.*, 2024, **6**, 546, DOI: 10.1007/s44247-024-00379-y.
113 A. T. Khalil, M. Ovais, I. Ullah, M. Ali, Z. K. Shinwari and M. Maaza, *Green Chem. Lett. Rev.*, 2017, **10**, 186–201, DOI: 10.1080/17518253.2017.1339831.
114 S. Ashrafi-Saiedlou, M. Rasouli-Sadaghiani and M. Fattahi, *Heliyon*, 2025, **11**, e33005, DOI: 10.1016/j.heliyon.2025.e33005.
115 A. A. Fayyadh, J. N. Makassees and A. K. Hattab, Acad, *Open*, 2025, **10**, 10–21070, DOI: 10.21070/acadopen.2025.10-21070.
116 T. H. Endres, A. A. Yimer, T. T. Beyene and G. G. Muleta, *Results Chem.*, 2025, **15**, 102184, DOI: 10.1016/j.rechem.2025.102184.
117 Y. P. Teoh, Z. X. Ooi, S. S. Leong, P. T. Ng and W. W. Liu, *J. Eng. Sci.*, 2021, **17**, 19–29.
118 J. Yoonus, R. Resmi and B. Beena, *Mater. Today Proc.*, 2021, **46**, 2969–2974, DOI: 10.1016/j.matpr.2020.12.426.
119 N. Z. Emami-Karvani, *Afr. J. Microbiol. Res.*, 2012, **5**, 1368–1373, DOI: 10.5897/AJMR10.159.
120 Y. Y. Loo, Y. Rukayadi, M.-A.-R. Nor-Khaizura, C. H. Kuan, B. W. Chieng, M. Nishibuchi and S. Radu, *Front. Microbiol.*, 2018, **9**, 1555, DOI: 10.3389/fmicb.2018.01555.
121 J. P. Ruparelia, A. K. Chatterjee, S. P. Duttagupta and S. Mukherji, *Acta Biomater.*, 2007, **4**, 707–716, DOI: 10.1016/j.actbio.2007.11.006.
122 R. B. Fulindi, J. D. Rodrigues, T. W. L. Barbosa, A. D. G. Garcia, F. De Almeida La Porta, S. Pratavieira, L. A. Chiavacci, J. P. Araújo Junior, P. I. Da Costa and L. R. Martinez, *Microbiol. Spectr.*, 2023, **11**, e04831–22, DOI: 10.1128/spectrum.04831-22.
123 A. Sharifi, A. Mohammadzadeh, T. Z. Salehi and P. Mahmoodi, *J. Appl. Microbiol.*, 2017, **124**, 379–388, DOI: 10.1111/jam.13639.
124 F. Alhosani, D. Islayem, S. Almansoori, A. Zaka, L. Nayfeh, A. Rezk, *et al.*, *Sci. Rep.*, 2025, **15**, 17321, DOI: 10.1038/s41598-025-02372-6.
125 A. Mitra, *Cell Surf.*, 2024, **12**, 100133, DOI: 10.1016/j.tcsw.2024.100133.

126 J. Lan, J. Zou, H. Xin, J. Sun, T. Han, M. Sun and M. Niu, *J. Contr. Release*, 2025, **400**, 113589, DOI: 10.1016/j.jconrel.2025.113589.
127 D. Das, B. C. Nath, P. Phukon and A. Kalita, *Colloids Surf., B*, 2013, **111**, 556–560, DOI: 10.1016/j.colsurfb.2013.06.041.
128 H. Chandra, D. Patel, P. Kumari, J. S. Jangwan and S. Yadav, *Mater. Sci. Eng., C*, 2019, **102**, 212–220, DOI: 10.1016/j.msec.2019.04.035.
129 T. Khan, M. Mazid and F. Mohammad, *Int. J. Astrobiol.*, 2011, **28**, 97–111, DOI: 10.2478/v10146-011-0011-x.
130 D. A. Lomelí-Rosales, A. Zamudio-Ojeda, O. K. Reyes-Maldonado, M. E. López-Reyes, G. C. Basulto-Padilla, E. J. Lopez-Naranjo, V. M. Zuñiga-Mayo and G. Velázquez-Juárez, *Molecules*, 2022, **27**, 1692, DOI: 10.3390/molecules27051692.
131 S. S. Awan, R. T. Khan, A. Mehmood, M. Hafeez, S. R. Abass, M. Nazir and M. Raffi, *Saudi J. Biol. Sci.*, 2022, **30**, 103487, DOI: 10.1016/j.sjbs.2022.103487.
132 N. Abbes, I. Bekri, M. Cheng, N. Sejri, M. Cheikhrouhou and J. Xu, *Mater. Sci.*, 2021, **28**, 144–150, DOI: 10.5755/j02.ms.28314.
133 P. Kumar, S. Kumar and N. Thakur, *Inorg. Chem. Commun.*, 2023, **155**, 111084, DOI: 10.1016/j.inoche.2023.111084.
134 S. T. Shah, W. A. Yehya, O. Saad, K. Simarani, Z. Chowdhury, A. A. Alhadi and L. A. Al-Ani, *Nanomaterials*, 2017, **7**, 306, DOI: 10.3390/nano7100306.
135 K. M. Lee, C. W. Lai, K. S. Ngai and J. C. Juan, *Water Res.*, 2015, **88**, 428–448, DOI: 10.1016/j.watres.2015.09.045.
136 M. Aminuzzaman, P. S. Ng, W. S. Goh, S. Ogawa and A. Watanabe, *Inorg. Nano-Met. Chem.*, 2019, **49**, 401–411, DOI: 10.1080/24701556.2019.1661464.
137 A. N. Abdulqodus, A. F. Abdulrahman and S. H. Mostafa, *Appl. Phys. A*, 2025, **131**, 720, DOI: 10.1007/s00339-025-08874-4.
138 M. Aliannezhadi, S. Z. Mirsanaee, M. Jamali and F. Shariatmadar Tehrani, *Sci. Rep.*, 2024, **14**, 2035, DOI: 10.1038/s41598-024-52455-z.
139 J. Lu, H. Ali, J. Hurh, Y. Han, I. Batjikh, E. J. Rupa, *et al.*, *Optik*, 2019, **184**, 82–89, DOI: 10.1016/j.ijleo.2019.03.050.
140 T. S. Aldeen, H. E. A. Mohamed and M. Maaza, *J. Phys. Chem. Solids*, 2022, **160**, 110313, DOI: 10.1016/j.jpcs.2021.110313.
141 X. Liu, Y. Yang, H. Li, Z. Yang and Y. Fang, *Chem. Eng. J.*, 2020, **408**, 127259, DOI: 10.1016/j.cej.2020.127259.
142 P. L. Meena, K. Poswal and A. K. Surela, *Water Environ. J.*, 2022, **36**, 513–524, DOI: 10.1111/wej.12783.
143 L. V. Trandafilović, D. J. Jovanović, X. Zhang, S. Ptasińska and M. D. Dramićanin, *Appl. Catal., B*, 2016, **203**, 740–752, DOI: 10.1016/j.apcatb.2016.10.063.
144 J. K. Park, E. J. Rupa, M. H. Arif, J. F. Li, G. Anandapadmanaban, J. P. Kang, M. Kim, J. C. Ahn, R. Akter, D. C. Yang and S. C. Kang, *Optik*, 2021, **239**, 166249, DOI: 10.1016/j.ijleo.2020.166249.
145 L. Jing, Z. Ji, J. Wang, J. Guo, S. Lu, J. Sun, L. Cai and Y. Wang, *Nanomaterials*, 2021, **11**, 2479, DOI: 10.3390/nano11102479.
146 T. Karnan and S. A. S. Selvakumar, *J. Mol. Struct.*, 2016, **1125**, 358–365, DOI: 10.1016/j.molstruc.2016.07.029.
147 H. Sadiq, F. Sher, S. Sehar, E. C. Lima, S. Zhang, H. M. N. Iqbal, F. Zafar and M. Nuhanović, *J. Mol. Liq.*, 2021, **335**, 116567, DOI: 10.1016/j.molliq.2021.116567.
148 V. V. Gawade, N. L. Gavade, H. M. Shinde, S. B. Babar, A. N. Kadam and K. M. Garadkar, *J. Mater. Sci.: Mater. Electron.*, 2017, **28**, 14033–14039, DOI: 10.1007/s10854-017-7254-2.
149 N. Rana, S. Chand and A. K. Gathania, *Int. Nano Lett.*, 2016, **6**, 91–98, DOI: 10.1007/s40089-015-0171-6.
150 S. A. Devi, K. J. Singh and K. N. Devi, *Integr. Ferroelectr.*, 2020, **205**, 38–51, DOI: 10.1080/10584587.2019.1674995.
151 M. B. Goudjil, H. Dali, S. Zighmi, Z. Mahcene and S. E. Bencheikh, *Desalination Water Treat.*, 2024, **317**, 100079, DOI: 10.1016/j.dwt.2024.100079.
152 A. Miri, A. S. Sedighi, A. Najafidoust, M. Khatami and M. Sarani, *Int. J. Environ. Anal. Chem.*, 2023, **103**, 8369–8383, DOI: 10.1080/03067319.2021.1986035.
153 N. Thakur, P. Kumar, A. Tapwal and K. Jeet, *Nanofabrication*, 2023, **8**, 1–12, DOI: 10.1016/j.nanofab.2023.08.001.
154 S. Kaushal, A. Kumar, H. Bains, *et al.*, *Environ. Sci. Pollut. Res.*, 2023, **30**, 37092–37104, DOI: 10.1007/s11356-022-24848-y.
155 S. Haseena, S. Shanavas, T. Ahamad, S. M. Alshehri, P. Baskaran, J. Duraimurugan, *et al.*, *J. Environ. Chem. Eng.*, 2021, **9**, 104996, DOI: 10.1016/j.jece.2020.104996.
156 T. Indumathi, N. Krishnamoorthy, R. Valarmathy, K. Saraswathi, S. Dilwyn and S. Prabhu, *Nano Biomed. Eng.*, 2022, **14**, 3.
157 W. Ahmad, V. Singh, S. Ahmed and M. Nur-e-Alam, *Results Eng.*, 2022, **14**, 100450, DOI: 10.1016/j.rineng.2022.100450.
158 A. Barapatre, K. R. Aadil and H. Jha, *Clean: Soil, Air, Water*, 2017, **45**, e600045, DOI: 10.1002/clen.201600045.
159 M. Nikitha, S. Sowndharya and S. Meenakshi, *J. Water Process Eng.*, 2024, **63**, 105571, DOI: 10.1016/j.jwpe.2024.105571.
160 I. Azad, T. Khan, A. K. Maurya, M. I. Azad and N. Mishra, *J. Mol. Recognit.*, 2021, **34**, e2918, DOI: 10.1002/jmr.2918.
161 J. Lee and L. Zhang, *Protein Cell*, 2014, **6**, 26–41, DOI: 10.1007/s13238-014-0100-x.
162 S. Datta, V. Singh, S. Nag and D. N. Roy, *Can. J. Microbiol.*, 2024, **70**, DOI: 10.1139/cjm-2024-0155.
163 N. Chowdhury and A. Bagchi, *Gene*, 2016, **580**, 80–87, DOI: 10.1016/j.gene.2015.12.067.
164 A. M. Hardman, G. S. A. B. Stewart and P. Williams, *Antonie van Leeuwenhoek*, 1998, **74**, 199–210, DOI: 10.1023/A:1001178702503.
165 E. C. Pesci, J. P. Pearson, P. C. Seed and B. H. Iglewski, *J. Bacteriol.*, 1997, **179**, 3127–3132, DOI: 10.1128/jb.179.10.3127-3132.1997.
166 O. Lidor, A. Al-Quntar, E. C. Pesci and D. Steinberg, *Sci. Rep.*, 2015, **5**, 16569, DOI: 10.1038/srep16569.
167 F. Lowy, *N. Engl. J. Med.*, 1998, **339**, 520–532, DOI: 10.1056/NEJM199808203390806.

168 B. Palaniappan, A. P. Solomon and D. R. C, *Life Sci.*, 2021, **273**, 119306, DOI: **10.1016/j.lfs.2021.119306**.
169 R. P. Novick, *Mol. Microbiol.*, 2003, **48**, 1429–1449, DOI: **10.1046/j.1365-2958.2003.03526.x**.
170 R. L. Koenig, J. L. Ray, S. J. Maleki, M. S. Smeltzer and B. K. Hurlburt, *J. Bacteriol.*, 2004, **186**, 7549–7555, DOI: **10.1128/jb.186.22.7549-7555.2004**.
171 L. Laganenka and V. Sourjik, *Isr. J. Chem.*, 2022, **63**, e202200080, DOI: **10.1002/ijch.202200080**.